

SIZING AND MODELING OF ELECTRIC POWERTRAINS FOR SMALL UNMANNED
AERIAL SYSTEMS

A Thesis

by

FARID SAEMI

Submitted to the Office of Graduate and Professional Studies of
Texas A&M University
in partial fulfillment of the requirements for the degree of
MASTER OF SCIENCE

Chair of Committee, Dr. Moble Benedict
Committee Members, Dr. Hamid Toliyat
Dr. Manoranjan Majji

Head of Department, Dr. Srinivas Vadali (Interim)

December 2020

Major Subject: Aerospace Engineering

Copyright 2020 Farid Saemi

ABSTRACT

The following describes development of performance models for the battery, motor controller (electronic speed controller, or ESC), and brushless DC (BLDC) motor of small unmanned aerial systems (UAS) with a gross takeoff weight less than 20 kg (55 lb). The thesis also develops a sizing algorithm for the brushless DC motor.

The performance models for the motor, ESC, and battery use component specifications to enable pre-conceptual design space exploration and mission-based design optimization of small UAS powertrains without a library of test data. The models also enable tradeoffs analysis between existing and conceptual designs without a series of flight tests. To develop, tune, and validate the models, a custom dynamometer test setup was designed and built to measure torque, speed, and electrical power data of brushless DC motor drive systems. The validated models, which could predict the combined motor/ESC efficiency within 5% points of experimental values, reveal that popular claims of "high efficiency" for electric powertrains are only valid in a narrow band of high speed/low torque operation.

Conversely, the sizing algorithm can predict the mass, geometry, and figure of merit (k_m) of a motor rated for a given torque. The algorithm can then predict the optimal torque constant (k_t), speed constant (k_v), and winding resistance (R) given an operating voltage and shaft speed. To develop and validate the algorithm, complementary theoretical and experimental methods were used to overcome two key barriers: (1) motor performance theory was used to generate non-existent performance data, and (2) empirical trends in motor design were leveraged to connect independent theoretical torque, volume, and mass models. The resulting mass and figure of merit predictions are within $\pm 20\%$ of actual values for motors ranging in mass from 25–500 g (1–18 oz.) and varying geometries. The validated algorithm also revealed that motor size (and therefore mass) grows with torque, not power.

DEDICATION

To my parents who have sacrificed so much for me.

Thank you.

ACKNOWLEDGMENTS

This is, for all intents and purposes, an electrical engineering problem applied to aerospace. So, I was "flying blind" for a good while until a few people helped me get my bearings.

My adviser Dr. Moble Benedict was always helpful in maintaining my overall heading. I have learned a lot from him, and I admire how he is a true aerospace engineer who has a strong fundamental grasp of fluid dynamics, structures, and dynamics & controls. I could not have asked for a better adviser in this field.

Motor researchers Matthew Gardner and Nima Ershad repeatedly helped me make sense of the electrical world I was flying into. They repeatedly took time out of their busy schedules to help me understand different concepts as I learned more about motor drives. I really could not have accomplished anything without their support. I would also like to thank Bruce Abbott, Charles Cowie, Richard Drummond, and a few other folks on Electrical Engineering Stack Exchange for patiently answering my questions.

I would not have been able to build or wire anything without the master of all trades, David Coleman. If I was ever unsure about how to do something in the lab, I always knew who to turn to. Thank you, David. On a similar hands-on note, I would not have even gotten exposed to this electrical world without Scott Tran. Sorry I roped you into research, buddy!

I would also like to thank my mentors and teachers going back to elementary school. I cannot help but feel I've had the privilege of learning from some smart and thoughtful folks. Teachers are nation builders, and I think I've lived in a great nation.

I would not have stayed (relatively) sane without the support of many dear friends who helped me through various academic and non-academic struggles. Thanks for dealing with me! Finally, thanks to my parents for coming and toiling in America for me to enjoy such life-changing opportunities. I need to hurry up and graduate so I can start paying y'all back!

CONTRIBUTORS AND FUNDING SOURCES

Contributors

This work was supported by a thesis committee consisting of Professors Moble Benedict (Chair) and Manoranjan Majji of the Department of Aerospace Engineering and Professor Hamid Toliyat of the Department of Electrical Engineering.

All work conducted for the thesis was completed by the student.

Funding Sources

This research was sponsored by the Army Research Laboratory and was accomplished under Cooperative Agreement Number W911NF-18-2-0274. The views and conclusions contained in this document are those of the authors and should not be interpreted as representing the official policies, either expressed or implied, of the Army Research Laboratory or the U.S. Government. The U.S. Government is authorized to reproduce and distribute reprints for Government purposes notwithstanding any copyright notation herein.

NOMENCLATURE

A	Area [m ²]
B	Magnetic flux density [T]
d	Duty ratio (throttle setting) [-]
D	Diameter [m]
DOD	Depth of discharge [%]
E	Back-electromotive force (back-EMF) [V]
f	Frequency [Hz]
F	Force [N]
I	Current [A]
J	Surface current density [A/m]
k_m	Motor constant [$\frac{N \cdot m}{\sqrt{\Omega}}$]
k_t	Torque constant [N·m/A]
k_v	Speed (voltage) constant [rev/(min·V)]
L	Length [m]
m	Mass [kg]
M	Torque [N·m]
N	Shaft speed [rev/min]
P	Power [W]
Q	Battery capacity [Ah]
R	Resistance [Ω]
SOC	State of charge [%]
T	Time [s]

U	Volume [m ³]
w	Width [m]
V	Voltage [V]
ζ	Resistivity [Ω /m]
η	Efficiency [%]
ρ	Density [kg/m ³]
σ	Shear stress [Pa]
ϕ	Motor phase lag [deg]
ω	Angular velocity [rad/s]

TABLE OF CONTENTS

	Page
ABSTRACT	ii
DEDICATION	iii
ACKNOWLEDGMENTS	iv
CONTRIBUTORS AND FUNDING SOURCES	v
NOMENCLATURE	vi
TABLE OF CONTENTS	viii
LIST OF FIGURES	x
LIST OF TABLES.....	xiii
1. INTRODUCTION.....	1
1.1 Motivation	1
1.2 Electric powertrain overview	2
1.3 Existing small UAS design tools	4
1.4 Contributions to the state of the art.....	6
1.5 Broader vision	7
1.6 Scope	8
1.7 Methodology	9
1.8 Summary	10
2. EXPERIMENTAL DATA COLLECTION	11
2.1 Eddy-current dynamometer.....	11
2.2 Battery analyzer	15
2.3 Hover stand.....	16
3. BRUSHLESS DC MOTOR.....	17
3.1 Primer.....	17
3.1.1 What is a motor?.....	17
3.1.2 What does a motor look like?	19
3.1.3 How does a motor work?.....	20
3.1.4 Torque versus size	21

3.1.4.1	Force on a wire	21
3.1.4.2	Force on a sheet	22
3.1.4.3	Torque on a cylinder.....	23
3.1.4.4	Motor torque.....	24
3.1.5	Steady state performance.....	27
3.2	Performance model	28
3.2.1	DC motor model.....	29
3.2.2	Accounting for magnetization losses	31
3.2.3	Accounting for harmonic losses	33
3.3	Sizing model.....	38
3.3.1	Initial attempts	39
3.3.2	Motor teardown.....	39
3.3.3	Prediction size and mass	41
3.3.4	Predicting electrical constants	50
3.4	Case study: High-speed versus high-torque motor	54
3.5	Summary	56
4.	ELECTRONIC SPEED CONTROLLER	59
4.1	Primer.....	59
4.2	Performance models	61
4.3	Hover stand validation	63
4.4	Summary	65
5.	BATTERY	67
5.1	Primer.....	67
5.2	Performance model	70
5.3	Benchtop internal resistance measurement	72
5.4	Summary	75
6.	CONCLUSION.....	76
6.1	Summary	76
6.1.1	Performance model summary.....	76
6.1.2	Sizing model summary	77
6.2	Contributions to literature	79
6.3	Future work.....	79
6.3.1	Re-vamped hoverstand testing	79
6.3.2	Other architectures	80
6.3.3	ESC and battery sizing models	80
6.3.4	Thermal modeling	80
6.3.5	Modeling at larger scales (> 1 kW).....	81
REFERENCES	82

LIST OF FIGURES

FIGURE	Page
1.1 Comparison of combustion and electric powertrains	3
1.2 Examples of all-electric small UAS	7
1.3 Example design framework	8
1.4 Modeling methodology	10
2.1 Custom dynamometer rig	12
2.2 Dynamometer test process	14
2.3 Sample dynamometer data	14
2.4 Sample battery discharge data	15
2.5 Hover stand setup	16
3.1 Motor diagram.....	17
3.2 Comparison of radial- and axial-flux motors	18
3.3 Comparison of outer- and inner-rotor motors.....	18
3.4 Sample BDLC motor.....	19
3.5 BLDC stator features.....	20
3.6 Stator windings.....	21
3.7 Lorenz force on a wire	22
3.8 Lorenz force on a sheet	23
3.9 Shear stress on sheet	23
3.10 Torque on a cylinder	24
3.11 Torque on a motor.....	25
3.12 Steady-state torque–speed graph	29

3.13 BLDC motor equivalent circuit v1	30
3.14 BLDC motor model v1 predictions	31
3.15 BLDC Motor equivalent circuit v2	32
3.16 BLDC motor model v2 predictions	33
3.17 Motor phase lag versus shaft speed	35
3.18 BLDC motor model v3 torque predictions.....	36
3.19 Motor waveform plots	37
3.20 BLDC motor model v3 efficiency predictions	38
3.21 BLDC motors of various size.....	40
3.22 Motor mass breakdown	41
3.23 KDE catalog torque versus mass, aspect ratio	42
3.24 KDE catalog torque versus stator volume, aspect ratio	42
3.25 KDE catalog with aspect ratio limit of 4.....	43
3.26 Overview of geometric mass model.....	44
3.27 Diameter ratio versus aspect ratio	45
3.28 Length ratio versus aspect ratio	45
3.29 Mass-prediction algorithm flow chart	46
3.30 Mass prediction given stator and outer dimensions	47
3.31 Mass prediction given stator dimensions.....	48
3.32 Mass prediction given torque and aspect ratio	49
3.33 Mass prediction of independent catalog.....	49
3.34 k_m predictions	52
3.35 R predictions	53
3.36 k_m prediction for independent catalog	53
3.37 R prediction for independent catalog	54

4.1	Simplified ESC commutation example.....	60
4.2	Reduced-order equivalent circuit	62
4.3	ESC efficiency predictions	63
4.4	Hover stand predictions	65
5.1	Lithium-ion battery diagram.....	67
5.2	State of charge (SOC) plots of common battery chemistries.....	69
5.3	Abu-Sharkh and Doerffel battery equivalent circuit	70
5.4	Reduced-order battery equivalent circuit.....	71
5.5	Battery model predictions	72
5.6	Pulse-discharge plot	74
5.7	Zoomed pulse-discharge plot	74

LIST OF TABLES

TABLE	Page
1.1 Department of Defense UAS classification table	2
3.1 Component densities averaged across 3 motor sizes	46
3.2 Comparison of high-speed and high-torque motors	55

1. INTRODUCTION



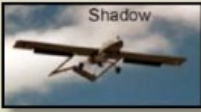

1.1 Motivation

The efficiency, scalability, and mechanical simplicity of electric motors has significantly expanded the designspace of modern aircraft. Modern aircraft designers are exploring a wide variety of concepts not seen since the early days of flight [1]. At large scales, new and established companies seem to announce different designs for a personal, commercial, or military electric vertical takeoff and landing (eVTOL) vehicle every day, such as the Google *Heaviside*, Bell *Nexus*, or XTI *Trifan*. At small scales, researchers are exploring even more radical concepts for unmanned aerial systems (UAS), such as biomimetic robotic hummingbirds [2], gust-tolerant cycloidal rotor micro aerial systems (MAV) [3], and optionally-recoverable gun-launched UAS [4].

The most mature and popular electric rotorcraft exist in this small scale as multi-rotor “drones” [5]. Consumers and professionals in a variety of industries use drones for recreation, remote inspection, and—increasingly—cargo delivery applications. Based on gross takeoff weight (GTOW), these all-electric vehicles fall within the group 1 and group 2 categories of the Department of Defense UAS classification system (Table. 1.1), and their powertrain components (motor, power electronics, battery) are typically sourced from the remote-control (RC) hobby world which popularized drones.

Unfortunately, group 1 and group 2 UAS are also designed with the hobby community’s heuristic rules of thumb, and the resulting small UAS designs can be highly suboptimal for a given mission, such as hover endurance. Over a three year period, systematic experimental optimization studies (+500 designs tested by varying rotor geometry, motors, and batteries) enabled the development of a 45 g (1.6 oz) quad-rotor based UAS at the University of Maryland [7] with almost double the electrical power loading (thrust per electrical power) of a comparable off-the-shelf system.

Table 1.1: Department of Defense UAS classification table (Credit: US Government [6])

UAS Groups	Maximum Weight (lbs) (MGTO)	Normal Operating Altitude (ft)	Speed (kts)	Representative UAS	
Group 1	0 – 20	<1200 AGL	100	Raven (RQ-11), WASP	
Group 2	21 – 55	<3500 AGL	< 250	ScanEagle	
Group 3	< 1320	< FL 180		Shadow (RQ-7B), Tier II / STUAS	
Group 4	>1320		> FL 180	Any Airspeed	Fire Scout (MQ-8B, RQ-8B), Predator (MQ-1A/B), Sky Warrior ERMP (MQ-1C)
Group 5		Reaper (MQ-9A), Global Hawk (RQ-4), BAMS (RQ-4N)			

1.2 Electric powertrain overview

Like combustion powertrains, electric powertrains simply convert stored chemical energy into mechanical power, but the subtle differences in the intermediary steps of this conversion—especially in the motor—cause confusion even in the electric machine community. The introduction of small UAS to the aerospace industry primarily from the technically non-rigorous hobby RC community has only exacerbated errors. This section aims to clear some misconceptions and establish baseline terms for the rest of the paper.

Figure 1.1 compares the components of an electric powertrain (power source, motor drive, and motor) to the components of a combustion powertrain. Both begin with a chemical source that provides power to the converter(s) which drive a mechanical load. In a combustion powertrain, the engine directly converts the fuel’s chemical energy into mechanical energy. In a typical electric powertrain, the *battery* source itself converts chemical energy into direct-current (DC) electrical

power for a second converter known as the motor drive or driver. The *driver* then converts the DC power into an alternating-current (AC) waveform of a specific voltage and frequency to the *motor* using feedback control algorithms and user inputs. The motor then converts this electrical power into mechanical power. The motor and driver are together known as the *motor drive system*.

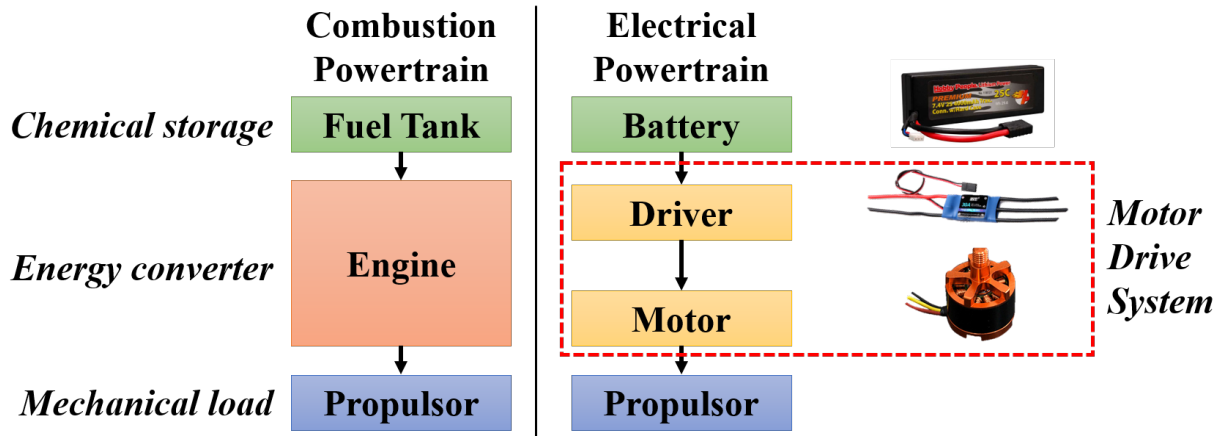


Figure 1.1: Comparison of combustion and electric powertrains (author figure)

Optimizing a powertrain requires a clear understanding of how constituent components' performance at the operating conditions affects overall power loss. For example, does increasing battery voltage to decrease current improve vehicle efficiency? Thus, the technical challenges to this work are:

1. Deriving physical models to predict components' performance at any design point and operating condition (e.g., motor torque at 5,000 rpm, 10 V_{DC}) using only high-level component specifications which are provided by most RC hobbyist manufacturers.
2. Quantifying the component power losses at each design point using idealized theoretical models
3. Applying limited empirical corrections to the output and efficiency prediction models that are related to underlying physical mechanisms rather than pure empirical trends.

1.3 Existing small UAS design tools

Obtaining even a fraction of such significant improvements through fast and cheap simulations rather than slow and costly experiments would provide a flexible framework for group 1 and group 2 UAS conceptual design [8]. This framework could then yield designs that optimally address the mission requirements of each UAS user. To deliver these results, the tool must not just simulate the performance of various subsystem configurations, like predicting motor torque at different speeds. The tool must also solve the inverse problem of sizing subsystems to meet performance requirements, like predicting the mass and size of a motor rated for a given torque [9].

Model-based design codes, like NASA Design and Analysis of Rotorcraft (NDARC), offer an example for improving the small UAS design process [10]. NDARC models different vehicle systems, such as the powertrain, as discrete modules. Each module can function in isolation or as part of a complete vehicle model. NDARC's semi-empirical modules were developed for combustion-based full-scale vehicles, so researchers have begun to develop similar tools for small electric UAS.

Some small UAS design tools, such as MIT's "Computational Multicopter Design" software [11] can optimize a multicopter's geometry for minimum weight and maximum controllability. Given certain specifications, such as the number of motors, motor spin directions, and motor arm lengths, the software will calculate a state-space model of the design and attempt to maximize the controllability matrix while minimizing mass. However, the user must provide the program with the vehicle's performance metrics, such as the rotor's thrust versus speed curve, the motor's power draw curve, and the battery's discharge curve. Such a conceptual design approach is impractical since: 1) a sub-optimal geometry with optimal powertrain parts may perform better than an optimal geometry with sub-optimal parts 2) the user must provide comprehensive test data for every powertrain configuration.

Researchers from the Army Research Laboratory (ARL) and Georgia Institute of Technology have developed a more systematic design tool, "Aggregate Derivative Approach to Product" (ADAPT), that can generate a small UAS design (fixed-wing or multi-copter) best-suited to high-

level user inputs, such as payload, speed, and endurance [12]. The tool uses physical models to derive power and energy requirements for the powertrain and the geometric layout before iteratively simulating different layout/component combinations to select the best-performing configuration. The design code then conducts a detailed design of the last-standing configuration in a computer-aided design (CAD) program to enable rapid delivery using commercial off-the-shelf (COTS) parts and additive manufacturing. However, ADAPt still relies on the user to provide empirical test data for each component (motor, battery, etc.) in a pre-existing library of parts. The software cannot simulate the performance of a configuration outside its pre-characterized designspace, so it cannot truly deliver the “optimal” vehicle configuration for a given mission.

Researchers at Maryland have developed a more robust mission-based small UAS design tool in the “HYbrid Design and Rotorcraft Analysis” (HYDRA) code [13]. HYDRA uses a combination of empirical weight studies, physics-based vehicle models, BEMT aerodynamic models, and FEA structural models to simulate vehicle dynamics and aerodynamic performance [14]. However, the program does not contain such physically-derived models for the electric powertrain. The powertrain efficiency is assumed to be constant for all flight conditions, and electrical performance is empirically derived. Therefore, the code cannot accurately predict the variation in an small UAS’s performance in different electrical operating conditions or configurations. Additionally, HYDRA’s sizing studies are all purely empirical, so they may not size components as accurately as the physics-based models in other modules.

In contrast, a core component of the NDARC full-scale design code is its engine module which uses a combination of semi-empirical models and empirical trends to comprehensively analyze the powertrain of a design [15]. Instead of test data, NDARC asks the user for high-level powertrain component specifications, such as specific fuel flow rate and rotor speed, and uses semi-empirical component models to predict performance under different operating conditions. Thus, the user does not need to conduct any component tests for one or a library of parts [16]. Data from the engine module will instead inform the user of the optimal engine specifications for the given mission. The engine module can also use semi-empirical sizing models to size the powertrain components’

mass, volume, and design specifications (such as specific fuel rate) to meet requirements derived elsewhere in NDARC from higher level design requirements.

Since group 1 and group 2 UAS are built around electric propulsion, a framework for the design of these UAS should rely on physics-based electric powertrain performance and sizing models. Moreover, the inputs and outputs of both models should be strategically coupled. For example, the motor sizing module should provide high level motor specifications that the performance model can use to validate the sizing module's prediction. Such coupling would ensure that every design iteration provides accurate feedback and drives the overall UAS concept design towards a global optimum.

1.4 Contributions to the state of the art

The following attempts to address the gap in physics-based electric powertrain modeling via:

1. **Performance models** that predict a component's steady-state output and efficiency using high-level specifications (not test data). [17]
2. **Sizing models** that predict the specifications of a component ideally rated to deliver a desired steady-state output.

The semi-empirical performance models for the battery, power electronics (electronic speed controllers or ESCs), and brushless DC (BLDC) motor use equivalent circuit theory and specifications like the battery's rated capacity or the motor's terminal resistance to predict:

1. Motor torque, current, and efficiency versus shaft speed at any operating voltage and throttle setting.
2. ESC current and efficiency versus shaft speed at any operating voltage and throttle setting.
3. Battery voltage versus time (state of charge) for a time-varying load.

The semi-empirical sizing model can predict the mass and electrical specifications of a motor rated to operate at a given torque and speed. The models consist of:

1. **Physically-derived expressions** that naturally scale for group 1 and group 2 UAS (Fig. 1.2).
2. **Empirically-tuned constants** that can be quickly reconfigured for a different class of machines.



(a) Consumer quadcopter
(credit: Nikita666, Wikimedia Commons)



(b) Delivery octocopter
(credit: HadasBandel, Wikimedia Commons)

Figure 1.2: Examples of all-electric small UAS (Credit: Wikimedia Commons)

1.5 Broader vision

The broader goal of this work is to develop an electric powertrain design module that models the scalability and flexibility that aircraft designers can leverage with electric motors. For example, two motors of similar mass but different length and diameter will deliver torque differently: one motor may take up less space while the other operates more efficiently. The module should predict such differences so that a higher-level design algorithm can select the motor that maximizes the larger system requirements—not simply motor efficiency.

Figure 1.3 illustrates how the proposed framework could work in the traditional systems engineering “V-model”. Given high-level user requirements (e.g., payload), a vehicle model would initially derive requirements for each sub-system (e.g., total thrust of the rotors). An aerodynamics module would size a suitable rotor to deliver this thrust and estimate the required torque and shaft speed. This information would then feed a powertrain module wherein the motor sizing algorithm

would size a motor rated for the torque and shaft speed. The algorithm would also predict the electrical constants of this motor which would enable performance models to verify that this hypothetical motor can actually deliver the required output. If so, the validated motor predictions would be passed back up to similar vehicle or aerodynamic performance models for further validation. Otherwise, the process would restart with different initial conditions. In an optimization scheme driven by multiple agents with random initial conditions (e.g., motor aspect ratio, number of rotors, battery voltage, etc.), the framework could find an unorthodox global optimum which fully utilizes the benefits of electric architecture rather than a local optimum born from traditional heuristics.

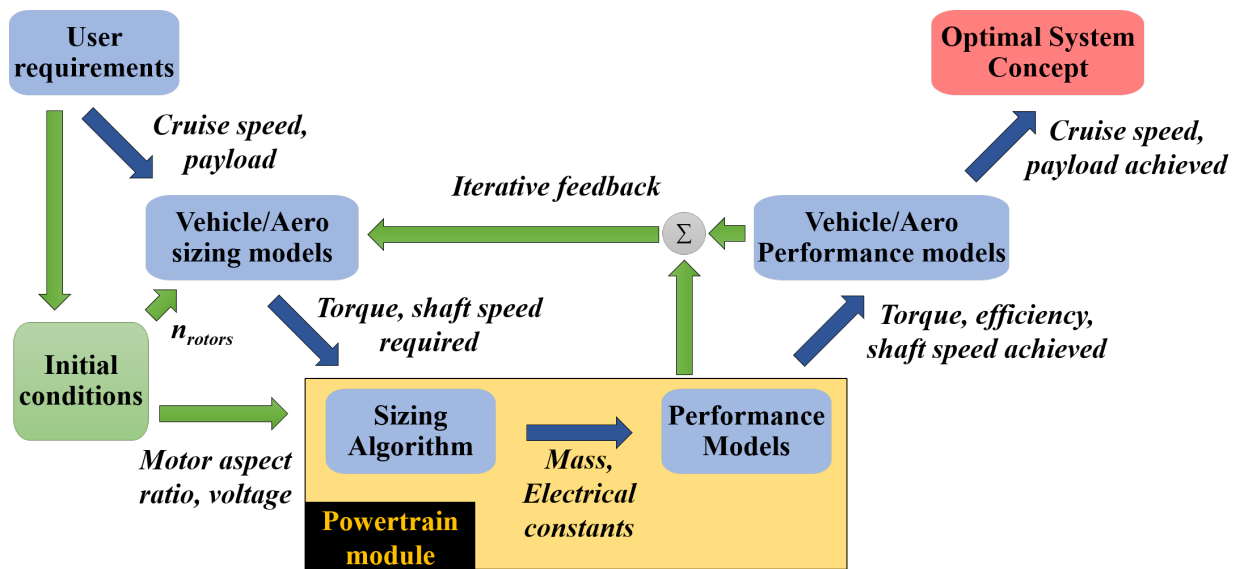


Figure 1.3: Example design framework (author figure)

1.6 Scope

The availability of certain data and the end-use of these models defines the scope of the work. For example, the performance model must estimate a motor's efficiency at different loads only using motor specs provided for cheap RC motors. The motor performance model cannot expect the user to provide inputs which come with premium industrial motors. Therefore, the performance model will not capture certain higher-order effects which require time-consuming and expensive

calibration, such as losses due to motor inductance. Similarly, the trends and conclusions of each chapter are limited to the type of component under study. For example, a reader should not apply the conclusions of the BLDC motor sizing model to induction or reluctance motors.

Broadly speaking, a reader can apply the trends and conclusions of each chapter as follows:

1. The motor performance and sizing models describe radial-flux, outer-rotor, permanent-magnet synchronous motors
2. The ESC performance model describes sensorless, six-step commutation motor controllers with PWM voltage control
3. The battery performance model describes high-discharge lithium-ion batteries with passive air-cooling (no thermal management)

1.7 Methodology

Figure 1.4 encapsulates the methodology used to develop the models in this work. First, a survey of electric machine literature provides a conceptual understanding of how each component works as well as a physically-derived expression for a component's behavior. Next, in-house experiments exposed the limitations of the theoretical model and provided hands-on exposure to how the component actually functioned. This insight then motivated empirical corrections or tuning of the theoretical model to better account for real-world behavior. The final result is a semi-empirical model whose underlying physics naturally scales with size. Moreover, the user can quickly reconfigure the model for other classes of components by changing the correction factors—not the entire expression.

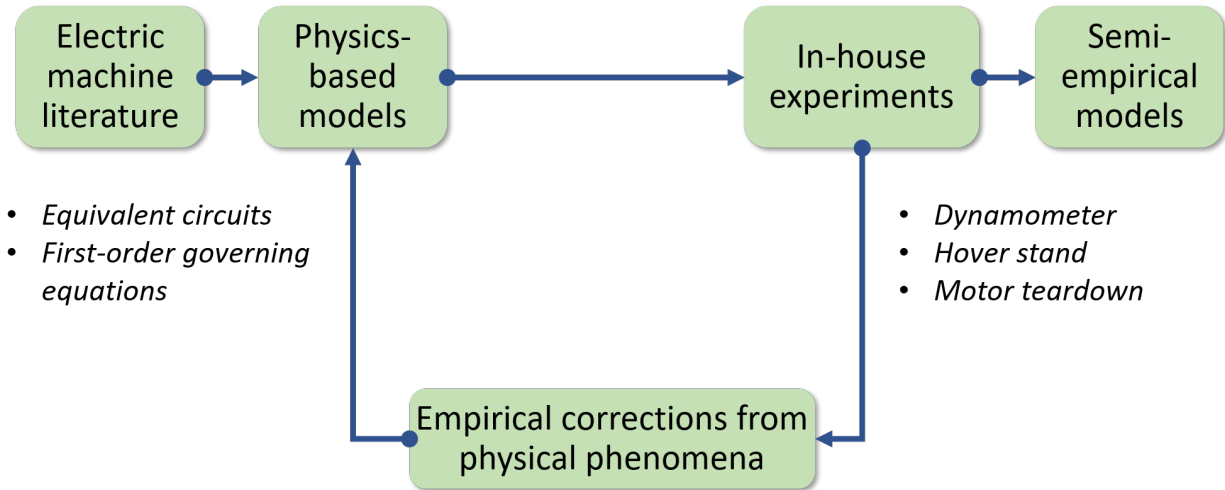


Figure 1.4: Modeling methodology (author figure)

1.8 Summary

Chapter 2 discusses all of the hardware that was used to gather the experimental data used in subsequent chapters. Chapters 3–5 discuss a single component (motor, ESC, and battery). The motor chapter (chapter 3) is the longest since it contains a performance model, a sizing model, as well as a case study. All other component chapters only contain a performance model. Each chapter begins with a primer that discusses how that component works before slowly building up the component model and comparing its results to experimental values. Each chapter concludes with a summary of the key results and a list of high-level takeaways. A final conclusion chapter collects the high-level summaries of chapters 3–5 and discusses future improvements.

2. EXPERIMENTAL DATA COLLECTION

A key challenge to this research was finding the necessary data to evaluate and validate the models with. For example, almost no brushless DC motor manufacturer provides any torque data for their motors¹. This lack of torque data prevented validation of the steady-state torque and speed performance model against a known truth. Therefore, many months of this research consisted of hardware design and experimental data collection.

2.1 Eddy-current dynamometer

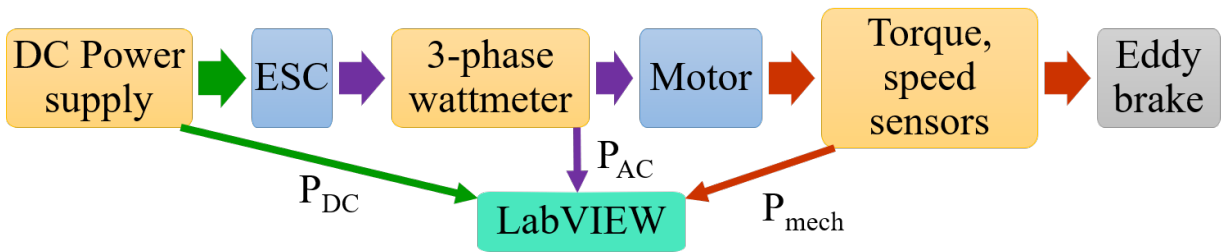
Most components for small electric UAS are sourced from the hobby RC community wherein little to no rigorous data exists about the performance and efficiency of each component. Some motor manufacturers, such as KDE Direct, publish propeller thrust versus drive system input power (DC voltage, current) data for select propeller, motor, and ESC combinations, but such data does not reveal anything about ESC efficiency, motor torque, or motor efficiency at different operating conditions. Manufacturers from mature industries, such as motors for automation systems, do provide efficiency versus speed plots for their motors, but these motors are typically part of heavy drive systems that are not suitable for aerospace applications. In the present study, experimental data had to be generated to develop, tune, and validate the semi-empirical models.

Characterizing the mechanical power output of a motor drive system requires loading the motor with torque independently of speed. Based on the difference between this load torque and the motor's available torque, the shaft's rotational speed will increase or decrease to a steady-state point on the motor's torque-speed curve. Varying the load torque while measuring steady-state torque and speed then reveals the entire motor torque-speed curve. A dynamometer ("dyno") is such a system that uses a braking mechanism to load an engine or motor and provide reading of torque, speed, and mechanical power. However, commercial dynamometers are expensive and not designed to operate at the sub-horsepower range of small UAS powertrains. Thus, the author built

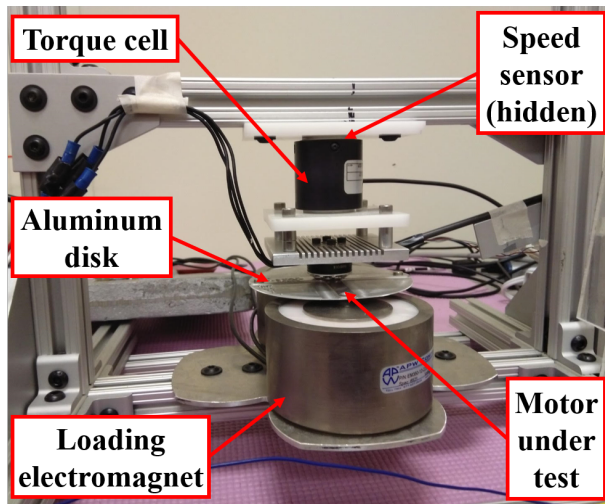
¹*T-Motors* seems to be a minor exception since it publishes torque data for some of its motors.

a custom dynamometer built using COTS components and sensors.

The dynamometer, abstracted in Fig. 2.1.a, consists of a magnetic brake (Fig. 2.1.b) to mechanically load a motor, a three-phase power analyzer² to record AC power between the ESC and motor, and a benchtop power supply to power to the ESC. A torque cell mounted in-line to the motor measures torque, and a laser speed sensor measures rotational speed. A LabVIEW program records torque, speed, and power readings streamed from the power analyzer and power supply to fully capture power across the motor drive system.



(a) Dynamometer block diagram



(b) Eddy-current brake

Figure 2.1: Custom dynamometer rig

The magnetic brake can supply a load torque independent of the motor speed. A separate DC

²Yokogawa WT333 3-element wattmeter

power source supplies current to an array of electromagnets underneath the motor. Their magnetic fields induce eddies of current into an aluminum disk spun by the motor. These eddy-currents then each generate their own magnetic field that opposes the external fields of the electromagnets, and the the repulsion between external and disk-based magnetic fields applies a torque on the motor. Increasing the electromagnets' supply voltage (and thereby current) increases this torque. The limiting conditions of this setup are the rated currents of the electromagnets and the rated power output of the load supply. Here, the drive system and eddy-brake are powered by identical 360 W (18 V, 20 A) variable voltage DC power supplies.

The presented dynamometer data are from tests of a 24 g KDE Direct 2304XF-2350 sensorless BLDC motor and a 10 g KDE UAS20LV ESC. This drive system was tested at 10% throttle increments for 50–100% throttle at 10 V and 12 V. The 50% lower limit was chosen since 50% throttle is the rule-of-thumb throttle setting for hover in the RC rotorcraft community. For each throttle setting, the motor was allowed to reach no-load steady state speed before the brake's input voltage was incremented 1 V every 5 seconds. Data was recorded continuously with clumps of data near the steady-state torque-speed point for each load voltage. Note, a DC power supply was used for the motor drive system instead of a battery to provide constant voltage during model development.

The measured motor output variables were torque (M) and rotational speed (N). The measured motor input/ESC output variables were three-phase active power (P_{AC}), three-phase apparent power (S), and one-phase RMS voltage (V_{RMS}) and RMS current (I_{RMS}). The measured ESC input variables were DC voltage (V_{DC}) and DC current (I_{DC}). The motor output power was calculated as the product of torque and angular velocity ($\omega = \pi N/30$). The motor input power/ESC output power was directly measured by the power analyzer as the active power. The ESC input power was calculated as the product of DC voltage and current. Figure 2.2 visualizes the test process and lists the measured data variables.

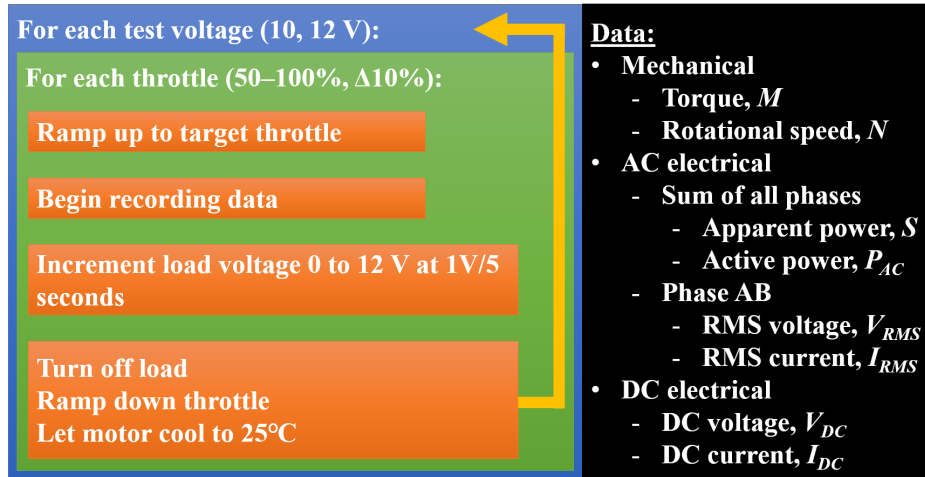


Figure 2.2: Dynamometer test process (author figure)

Figure 2.3 shows data for the 10 V test where only three throttle settings have been plotted for clarity. The motor trades torque for speed so that motor efficiency increases drastically with speed up to some peak value. The ESC exhibits a similar, although noisier, trend. Both motor and ESC efficiency improve at all speeds for higher throttle (or duty ratio) settings.

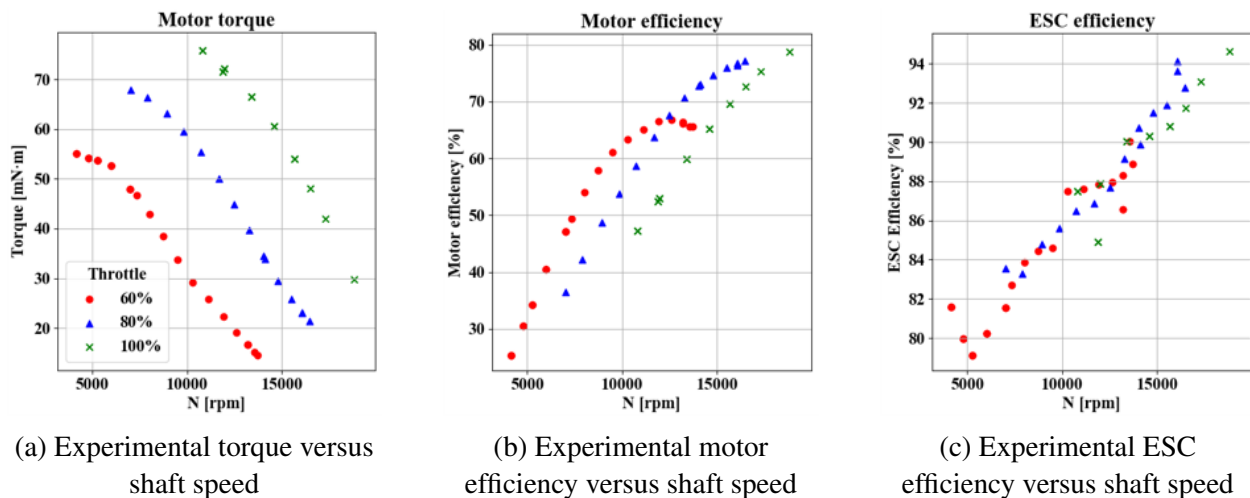


Figure 2.3: Sample dynamometer data (10 V_{DC})

Note, the load required to spin the aluminum disk with no braking imposes a lower speed limit on the motor than back-EMF. Assuming the disk load is proportional to the square of rotational speed, the motor's excess torque at high speed will grow smaller even as the DC source supplies higher voltage to overcome back-EMF. That is why each throttle curve never reaches the maximum rotational speed imposed by back-EMF.

2.2 Battery analyzer

A digital battery analyzer was used to discharge batteries at different rates (e.g., constant- or pulse-discharge currents) and record their voltage versus the relative discharged capacity of the battery (depth of discharge, or *DOD*). Both test methods were used to validate battery models. Figure 2.4 shows the variation of per-cell voltage versus depth of discharge at different discharge rates (*C*-value) for a 2S 740 mAh battery. Note the voltage begins to drop off more significantly around 80% *DOD* for the 1C and 2C cases which is why 80% *DOD* is the recommended lower limit for batteries in the RC community. Note also that the area under the curve—which represents the battery's total energy—of the 4C test is only 64% of the area under the curve of the 1C test. This denotes the significant internal losses of the battery at high discharge rates.

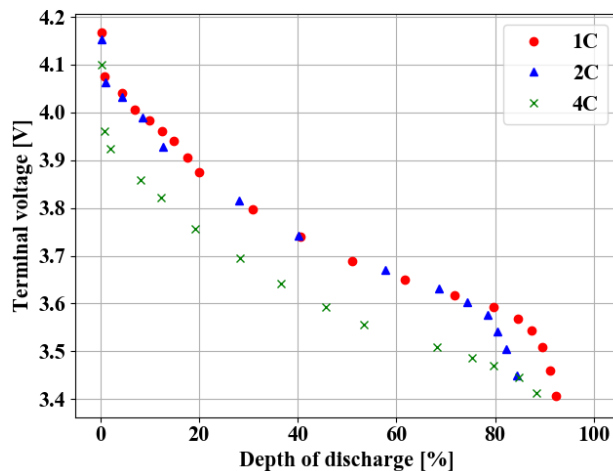


Figure 2.4: Sample battery discharge data ($V_{cutoff} = 3.3 \text{ V}$)

2.3 Hover stand

A hover test stand was used in order to validate the integrated motor drive system (motor+ESC) model against aerodynamic loads. The stand was instrumented with a laser angular velocity sensor and a power analyzer. The same DC power supply was used to power the hover stand that was used for the dynamometer. A combined force and torque cell measured rotor thrust and torque. The hover stand is pictured in Fig. 2.5.

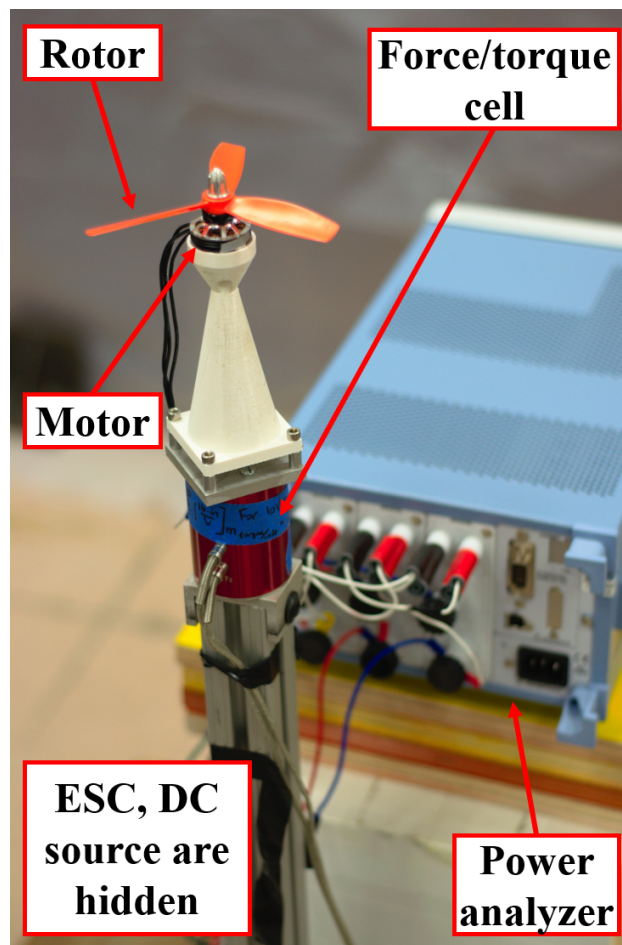


Figure 2.5: Hover stand setup

3. BRUSHLESS DC MOTOR

3.1 Primer

The following section aims to introduce readers with no context of electric motors to basic motor fundamentals.

3.1.1 What is a motor?

A motor is an *electric machine* that converts electrical power from a stationary *stator* into mechanical power on a rotating *rotor* via magnetic forces in the *airgap* between the stator and rotor (Fig. 3.1). Operated in the reverse manner (mechanical to electrical), the same machine serves as a generator. Therefore, the same models can describe motors and generators.

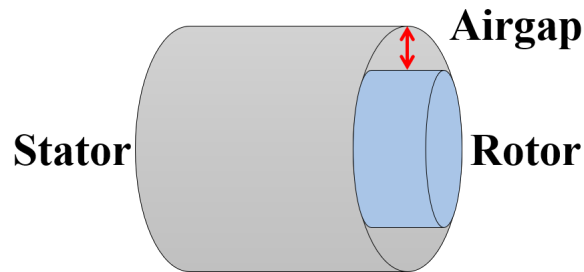


Figure 3.1: Motor diagram (author figure)

Designers may classify motors by their magnetic, mechanical, and electrical characteristics. The axis in which a motor generates and bounds magnetic field lines into a *magnetic flux* for power conversion is an important distinction. *Radial flux* motors are easier to manufacture and are the most common, but the electric vertical takeoff landing (eVTOL) community has stimulated development of *axial flux* motors which can generate more torque per unit mass [18, 19]. Figure 3.2 illustrates the differences in these divisions.

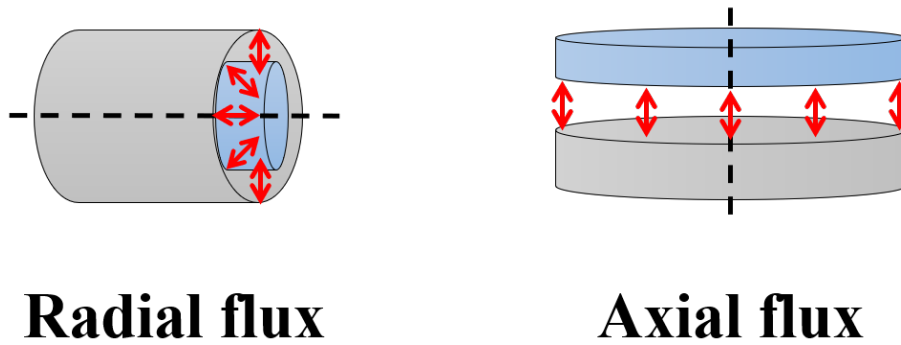


Figure 3.2: Comparison of radial- and axial-flux motors (author figure)

Separating motors by how their magnetic fields link the rotor and stator yields slightly more popular descriptions like “induction”, “reluctance”, and “synchronous” motors. Whether the rotor spins inside or outside the stator (*inrunner* or *outrunner* in hobby parlance) serves as yet another separator as depicted in Fig. 3.3. The ability to connect a motor directly to DC or AC power is a popular but inaccurate distinction. Modern high efficiency motors all rely on specially conditioned power from an intermediary power electronics unit ¹.

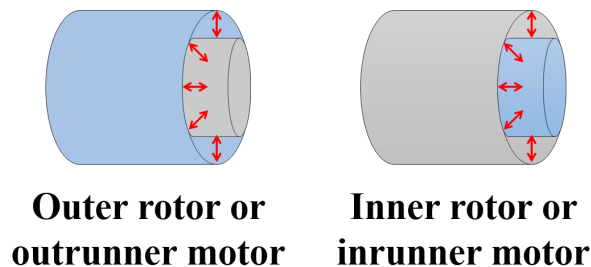


Figure 3.3: Comparison of outer- and inner-rotor motors (author figure)

This thesis focuses on the outrunner brushless DC motor most common to small electric UAS. In the electric machine community, these machines are defined as outer-rotor, radial-flux,

¹Brushless “DC” is a poor name for this reason. The electronic speed controller (ESC) converts battery DC power to AC power for the motor.

permanent-magnet synchronous motors. Research by Mevey [20] is an excellent starting point to learn about other motor types and unlearn common misconceptions. Text by Hughes and Drury [21] provides still more detail into the more general topic of *motor drive systems* which encompasses the motor and its associated power and control electronics.

3.1.2 What does a motor look like?

A BLDC motor consists of a cylindrical stator and rotor which spins around the stator as pictured in Fig. 3.4. A bolt pattern in the support structure at the back of the stator, as shown in the bottom right of Fig. 3.4, connects the motor to the rest of the system. A similar structure at the front of the rotor (Fig. 3.4 bottom left) supports a shaft which attaches to the load (e.g., a propeller). The shaft extends back through bearings at the front and end of the stator, and these bearings permit the rotor to spin while transferring axial and radial forces to the larger system.

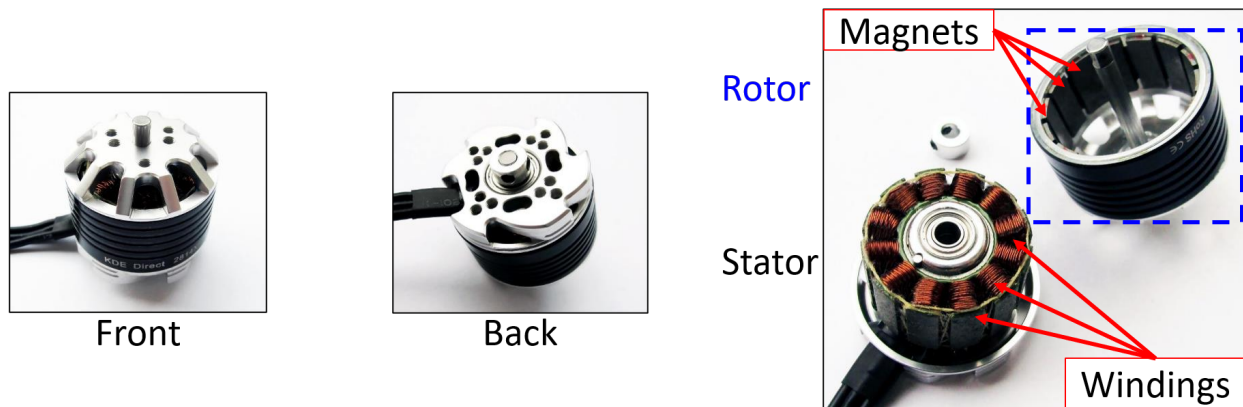


Figure 3.4: Sample BLDC motor (*KDE Direct 2814XF-515*)

Viewed from the front, the stator holds spokes of steel called *teeth* that extend to the back of the motor. Early motor teeth were made of iron, so together the teeth compose the *iron core* of a motor. Copper wire wound around each tooth develops the teeth into electromagnets called *windings*. Figure 3.5 shows the salient features and cross-section of a stator. The rotor houses a ring of permanent magnets or *poles* that wrap around the stator's lateral surface area.

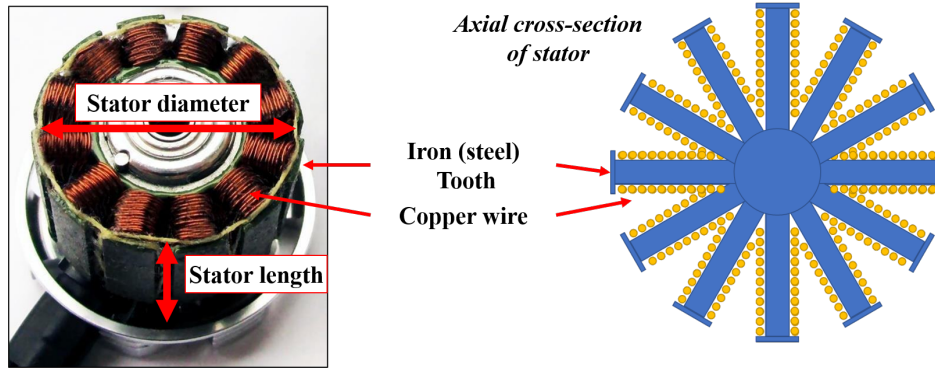


Figure 3.5: BLDC stator features (author figure)

3.1.3 How does a motor work?

A brushless DC motor's windings are wired into three sets or phases. Although a BLDC motor has three phases, the motor does not use all of the windings simultaneously. A single flow of current enters the stator through one set of windings (phase) and exits through another set of windings (phase) to develop a magnetic field in the stator. Timely energization of different combinations of phases on the stator revolves the stator's magnetic field, and the permanent magnets on the rotor follow the stator's field. The magnetic forces between stator electromagnets and rotor permanent magnets generate a torque on the shaft.

The subsequent interaction between the stator and rotor magnetic fields induces a voltage in the windings that generally opposes the input current. Consequently, this voltage is called "back-electromotive force" (back-EMF, E). Faster rotation speeds correspond to more frequent field interactions and a stronger back-EMF, so E imposes an electric speed limit for a motor. The dynamic E waveform in the unused winding can also roughly reveal rotor position which is critical to BLDC drivers. The strength of stator-rotor field interaction is captured by the motor constant, k_t . The constant is a function of the motor's design parameters (rotor magnet material, number of wire loops per winding, rotor shape, etc.). Figure 3.6 shows the "wye" (Y) configuration of the three BLDC phases (A, B, and C) and illustrates the back-EMF concept.

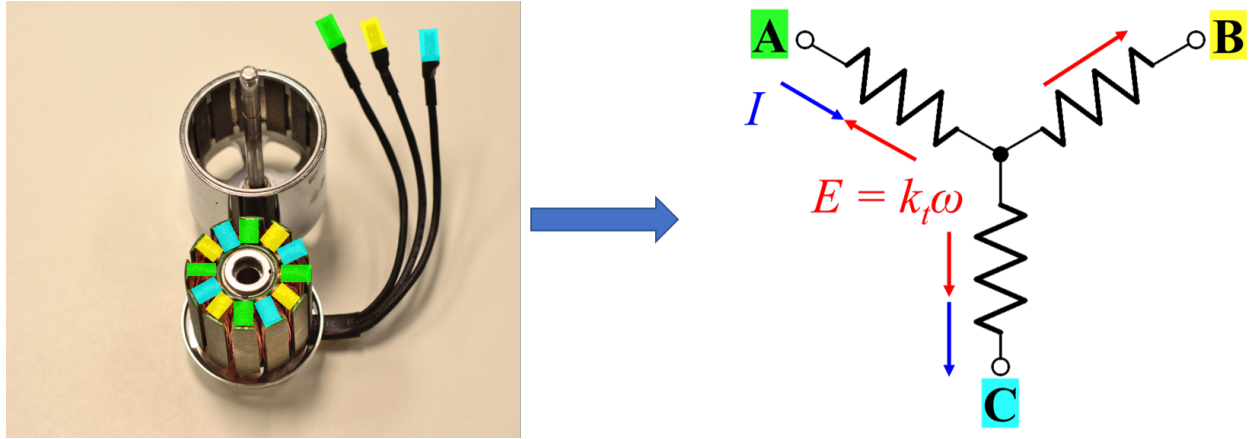


Figure 3.6: Stator windings (author figure)

3.1.4 Torque versus size

A physical expression relating torque to stator size can be derived by starting with the magnetic force on a single wire in a magnetic field and extending this to a cylindrical sheet of wires inside a magnetic field. [22].

3.1.4.1 Force on a wire

A wire conducting current in a magnetic field will experience the *Lorentz* force expressed in eq. 3.1 and illustrated in Fig. 3.7. The force is the cross product of the current-length vector IL and the flux density vector B of the field. The force points out of the page.

$$F_{wire} = IL \times B \quad (3.1)$$

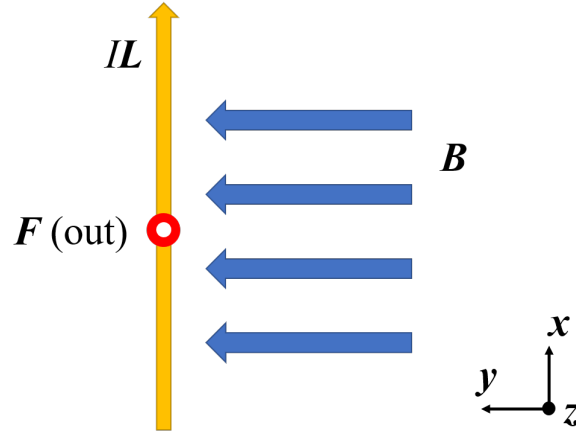


Figure 3.7: Lorentz force on a wire (author figure)

3.1.4.2 Force on a sheet

Connecting n such wires to a rigid sheet of length L and width w in the same magnetic field will scale the force by n as shown in eq. 3.2 and illustrated in Fig. 3.8. The area A of the current sheet can be used to define a tangential *shear stress* of magnitude BJ where J is the average current along the sheet width, or the *surface current density*. Some texts refer to B and J as *magnetic loading* and *electric loading* respectively.

$$\mathbf{F}_{sheet} = nIL \times \mathbf{B} \quad (3.2)$$

$$\sigma = F/A$$

$$\sigma = (nILB)/(Lw)$$

$$\sigma = (nIB)/w = B(nI/w)$$

$$\sigma = BJ \quad (3.3)$$

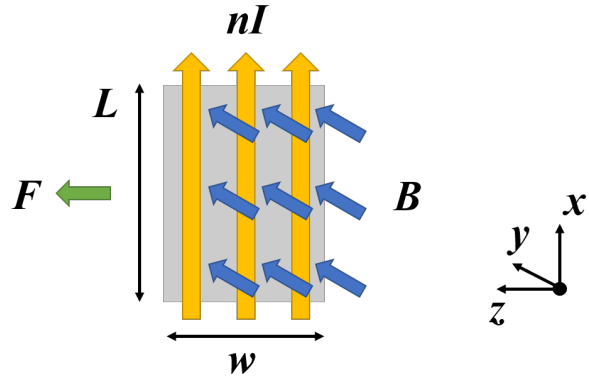


Figure 3.8: Lorenz force on a sheet (author figure)

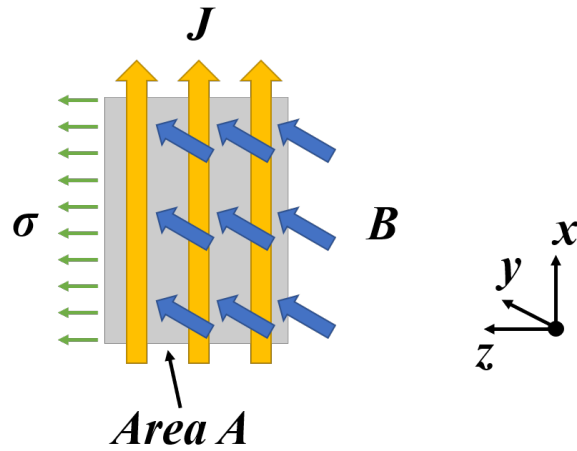


Figure 3.9: Shear stress on sheet (author figure)

3.1.4.3 Torque on a cylinder

Sweeping the sheet about a central axis creates a current cylinder with a uniform magnetic field normal to its lateral surface area as illustrated in Fig. 3.10. Measured about the central axis, the tangential shear stress on the surface area applies a force with a moment arm of $D/2$ to generate torque as derived in eq. 3.4. Note, surface current density is now defined as $J = nI/(\pi DL)$.

$$\begin{aligned}
 M &= F(D/2) \\
 M &= (\sigma A)(D/2) \\
 M &= (BJ)(\pi DL)(D/2) \\
 M &= \frac{\pi}{2}BJD^2L
 \end{aligned}
 \tag{3.4}$$

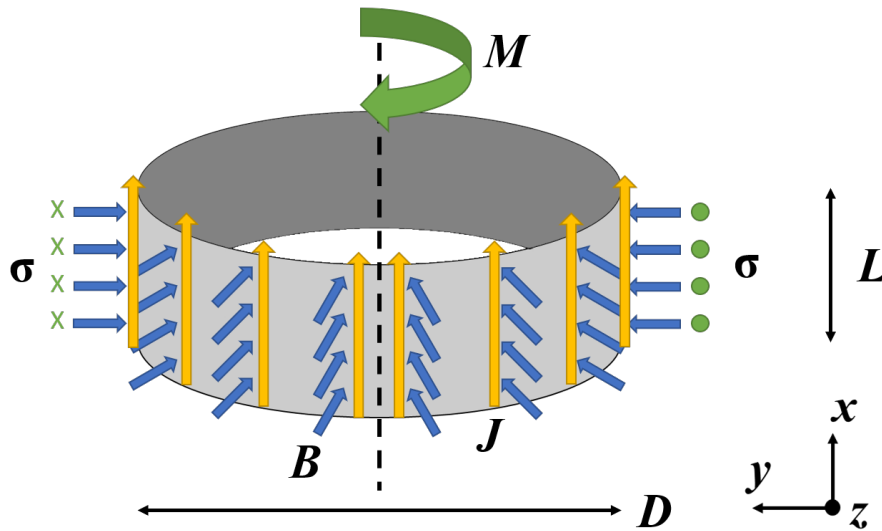


Figure 3.10: Torque applied to current cylinder in the $-x$ direction. The shear stress is out of the page $+z$ on the left side of the cylinder and into the page $-z$ on the right side of the cylinder (author figure)

3.1.4.4 Motor torque

The Lorentz force that applies a torque on the current cylinder applies an equal and opposite torque on the source of the magnetic field. This source could be a ring of permanent magnets with a surface area approximately equal to the cylinder's surface area. If the cylinder was fixed and the ring was free to rotate, the reaction torque on the ring could spin the ring and anything attached to

it (i.e., a shaft). From this point of view, the stationary current cylinder (stator) is applying a torque on the rotating magnet ring (rotor) as depicted in Fig. 3.11.

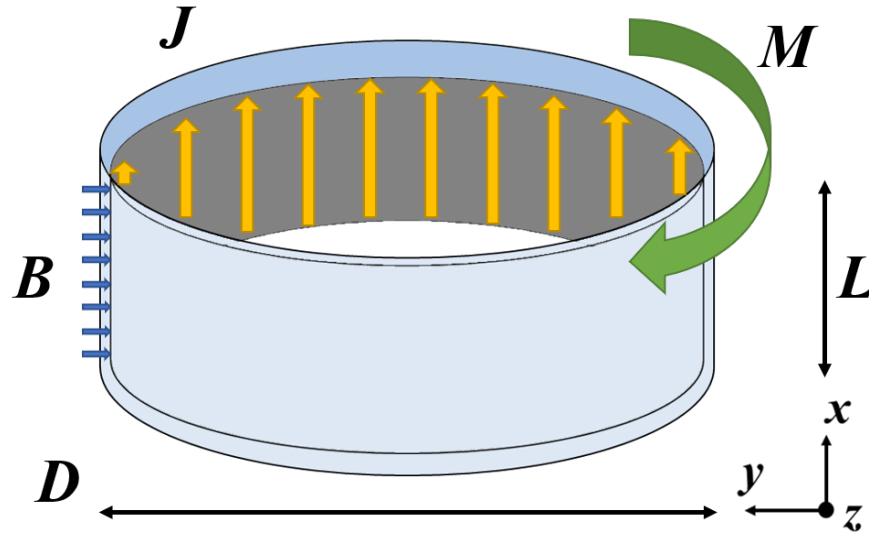


Figure 3.11: Torque applied to outer permanent magnet rotor (blue) in the $-x$ direction. The rotor provides the magnetic field which interacts with the stator's conductors (author figure)

If stator wires are wound around radial teeth rather than arranged as a thin sheet at the airgap, then the stator can fit more wires. The magnetically permeable teeth relay the rotor's magnetic field lines to the radially inner wires and permit these wires to interact with the rotor as well. Thus, windings increase the surface current density apparent at the airgap and thereby increase the developed torque.

Equation 3.11 can now be re-written as a function of the stator volume (U). The new expression in eq. 3.5 shows that torque is linearly proportional to the stator volume by a factor of 2σ . Note that torque is still developed at the lateral surface interface between the rotor and stator, i.e., torque is developed at the airgap. An inner-rotor/external-stator motor with an active lateral surface area of the same diameter and length, equal magnetic flux density from the rotor, and equal surface current density in the surrounding stator would develop the same amount of torque. Therefore,

the electric machine community expresses the relationship in eq. 3.5 in terms of the airgap to encompass motors of all rotor/stator arrangements (eq. 3.6).

$$\begin{aligned}
 M &= \frac{\pi}{2}BJD^2L \\
 M &= BJ\left(\frac{\pi}{2}D^2L\right) \\
 M &= (2)BJ\left(\frac{1}{2}\right)\frac{\pi}{2}D^2L \\
 M &= 2BJ\left(\frac{\pi}{4}D^2L\right) \\
 M &= 2BJU \\
 M &= 2\sigma U \tag{3.5}
 \end{aligned}$$

$$\begin{aligned}
 M &= \pi B_g J_g D_g^2 L_g \\
 M &= 2B_g J_g U_g \\
 M &= 2\sigma_g U_g \tag{3.6}
 \end{aligned}$$

The theoretical derivations presented so far assume that the magnetic flux density and the surface current density are not themselves functions of the motor size and geometry. This is not true in reality. For example, the steel teeth in a small motor may magnetically saturate before they can relay all of the magnetic flux from permanent magnets near the airgap to the wires at the stator core—thereby decreasing the real flux density of the motor [23]. A smaller motor may have less surface current density since the "windable" space between teeth decreases with size. Nevertheless, eq. 3.5 can be abstracted as a function of 3 factors:

1. **Geometry (D, L):** Increasing length and diameter increases the surface area of magnetic interactions and thereby the forces between the rotor and stator. Increasing diameter also increases the moment arm at which the forces develop torque.

2. **Material properties (B):** Manufacturers can make rare-earth permanent magnets with magnetic flux densities up to 1.5 tesla (T) at room temperature, but the hotter temperatures inside a motor practically limit magnetic loading to 1 T for BLDC motors.
3. **Environment (J):** Windings generate heat through I^2R losses. This heat will begin to increase the windings' resistance and degrade the rotor magnets' magnetic properties (B). Without sufficient cooling, I^2R losses may melt wire insulation and short the stator or heat rotor magnets above their *Curie temperature*² and permanently demagnetize the rotor. Liquid cooling may permit surface current densities up to 20 A/mm for a few seconds [24].

Two key parameters that have not yet appeared in this section are voltage and speed. That is because a motor of any size can theoretically operate at any speed provided sufficient input voltage. In other words, two motors with identical B , J , and D^2L —and thereby T —can deliver different power levels if one is supplied with a higher voltage. Therefore, a motor's size is weakly related to its power since a small, high-speed motor can deliver as much power as a large, high-torque motor. In fact, a motor will actually deliver power more efficiently at high-speed/low-torque [25], so a typical hybrid or electric car will still use a single-stage transmission to reduce motor torque requirements and thereby size [26].

3.1.5 Steady state performance

Figure 3.12 plots the natural (dashed) and rated (solid) response of a BLDC motor. Under ideal conditions of perfect control, perfect cooling, zero magnetic saturation, etc., the motor will naturally trade torque for speed up to a max speed or until the load torque matches the available torque (steady state). Equivalent circuit models can predict the natural torque-speed and efficiency-speed curve of BLDC motors using the electrical constants of the motor:

1. **Torque constant, k_t [N·m/A]:** Analogous to the slope of a wing's lift curve (C_{L_α}), k_t is defined as the slope of a motor's output torque versus input current. A motor's k_t is nominally

²The Curie point is the temperature above which certain materials lose their permanent magnetic properties

constant but will decrease as the motor’s iron core saturates (or magnetically “stalls”) or as the motor’s magnets demagnetize.

2. **Speed constant** k_v [rpm/V]: The slope of output speed to input voltage, k_v is the mathematical inverse of k_t when units are adjusted for.
3. **Winding resistance**, R [Ω]: The electrical resistance of the motor’s windings. I^2R loss from wire resistance is the greatest contributor to heat generated in the stator. This heat can further increase R and cause a positive feedback loop on motor temperature.

The rated response is more informative but more difficult to obtain because a manufacturer must use a precision motor controller, a dynamometer with a wide torque and speed band, and an appropriate cooling system to characterize the motor’s thermal and electromagnetic response to varying loads. The manufacturer will set a *rated torque* at which the motor can continuously operate and a *rated speed* up to which the motor can deliver rated torque. The manufacturer will test for a *maximum torque* at which the motor may operate for a defined short period of time before overheating, demagnetizing, or both. Some motor controllers are capable of weakening the magnetic fields inside a motor in such a way that the motor can spin faster than its natural maximum speed. Therefore, the manufacturer will also test for a *maximum speed* for the *field-weakening* zone of operation [20].

3.2 Performance model

Equivalent circuit diagrams are the “free body diagrams” of electrical engineering. Complex, multi-domain systems can be abstracted into a combination of ideal electric elements, such as resistors, sources, and switches, whose behavior can be expressed as mathematical functions. The primary challenge in this work was identifying non-ideal losses in each powertrain component and representing the losses using circuit elements. The turn key testing with the in-house dynamometer provided reliable experimental data that is lacking in literature for this analysis. The secondary challenge was applying empirical corrections to the governing expressions without requiring empirical data from the end-user. An oscilloscope, especially its current probe, enabled direct obser-

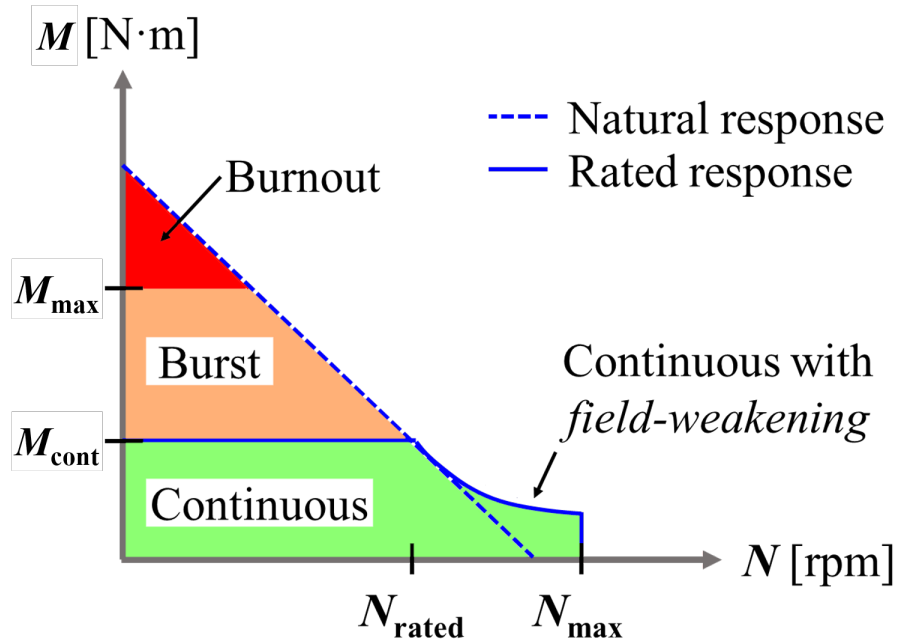


Figure 3.12: Steady-state torque–speed graph

variations of the working waveforms in a motor drive system which helped intuit correction factors based on physical changes rather numerical trends.

3.2.1 DC motor model

Since a single phase of current flows through two of three windings in a sensorless BLDC motor at any time, the equivalent circuit of a brushed DC motor [27] can model the operation of a brushless DC motor as well. The brushed circuit shown in Fig. 3.13 consists of two DC voltage sources and a resistor. The source on the left (V_{DC}) represents an externally applied voltage from which current flows. The source on the right (E) represents the back-EMF generated by motor that will resist the applied voltage. The resistor (R_m) represents the average winding-to-winding resistance between the three sets of windings (R_{ab} , R_{ac} , R_{bc}) in the motor. Current flows from the positive terminal of V_{DC} through R_m and E until $E = V_{DC}$.

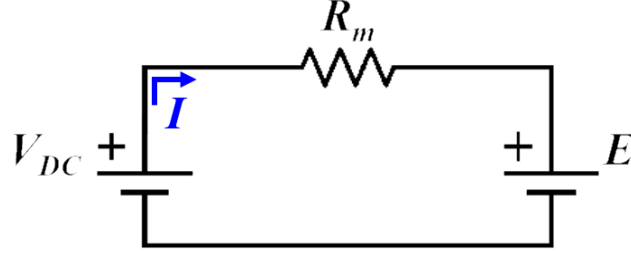


Figure 3.13: BLDC motor equivalent circuit v1

Applying Kirchhoff's Voltage Law to this current path yields Eq. 3.7 where duty ratio d (throttle setting divided by 100%) has been included to scale V_{DC} . The motor constant k_t linearly relates current to torque and back-EMF to angular velocity ($M = k_t I$, $E = k_t \omega$). This inter-domain parameter is provided by manufacturers, although some manufacturers provide the inverse parameter, k_v , which can be used to quickly obtain the maximum no-load speed at a given voltage ($N_{max} = k_v V_{DC} d$). Substituting and re-arranging terms in Eq. 3.7 yields the torque-speed equation for DC motors (Eq. 3.8). The torque and current can then be used to estimate output and input power which yields a measure of motor efficiency versus speed Eq. 3.9. Note, the current flowing through the motor is simply the predicted torque divided by k_t (Eq. 3.10).

$$V_{DC}d = IR_m + E \quad (3.7)$$

$$M_1 = \frac{V_{DC}dk_t - k_t^2\omega}{R_m} \quad (3.8)$$

$$\eta_1 = \frac{P_{out}}{P_{in}} = \frac{M_1\omega}{M_1\omega + I^2R_m} \quad (3.9)$$

$$I = \frac{M_1}{k_t} \quad (3.10)$$

Figure 3.14 shows the torque-speed (top) and efficiency-speed (bottom) model predictions

along with experimental values. Only the curves for 50% and 100% throttle have been plotted to clearly show the change in performance. The torque model trends very well and captures the tradeoff between torque and speed as growing back-EMF limits the torque-producing current entering the motor. When E equals V_{DC} , no more current enters the windings and the motor will reach maximum speed ($\omega_{max} = \frac{dV_{DC}}{k_t}$). However, the efficiency model does not peak at any speed and fails to predict the increased efficiency at higher throttle which indicate losses from high speed and low throttle respectively.

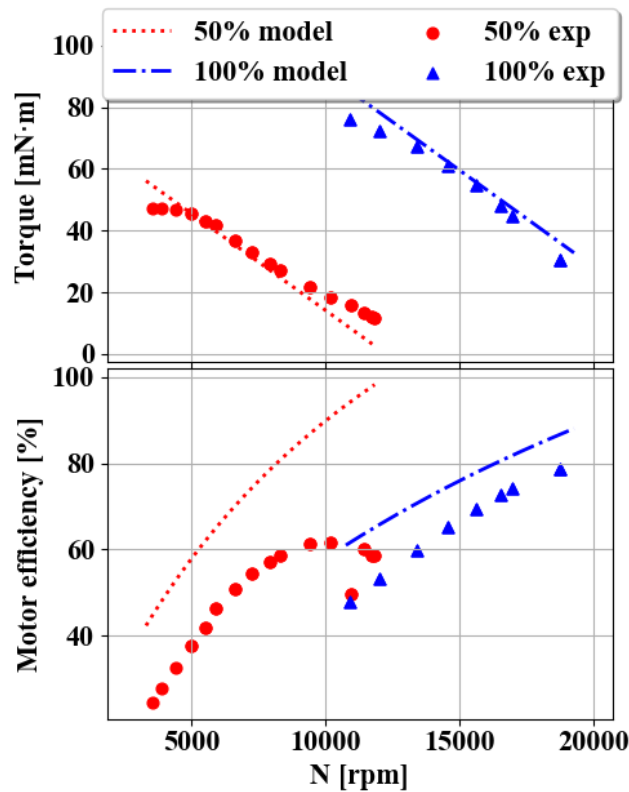


Figure 3.14: BLDC motor model v1 predictions ($V_{DC} = 10$ V)

3.2.2 Accounting for magnetization losses

The motor losses at high speed can be modeled by incorporating a magnetization penalty. The windings in a motor are looped around slots of an iron core. The iron greatly augments the strength

of the magnetic field generated by the winding current, but extra current must be expended to magnetize the iron in the proper orientation for each commutation cycle. This expenditure occurs more frequently with speed as the ESC commutates faster to keep the internal fields in sync.

The equivalent circuit in Fig. 3.15 contains a constant current source on the RHS that models the no-load current (I_0) that must be expended to energize the windings and magnetize the iron core [27]. Since $P = VI$, and the voltage across the parallel E and I_0 elements is the same, a new power loss term EI_0 that grows with speed can be incorporated into the efficiency model previously derived in Eq. 3.9. The addition of no-load current does not impact torque-speed predictions since the no-load current is added to the current derived from the torque-speed model (Eq. 3.12). The improved efficiency model (Eq. 3.11) plotted in Fig. 3.16 manages to predict the speed at which the 50% throttle curve reaches peak efficiency.

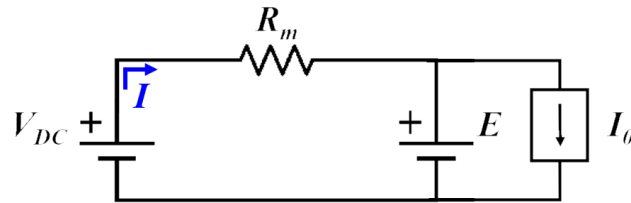


Figure 3.15: BLDC Motor equivalent circuit v2

$$\eta_2 = \frac{P_{out}}{P_{in}} = \frac{M_1\omega}{M_1\omega + I^2 R_m + k_t\omega I_0} \quad (3.11)$$

$$I = \frac{M_1}{k_t} + I_0 \quad (3.12)$$

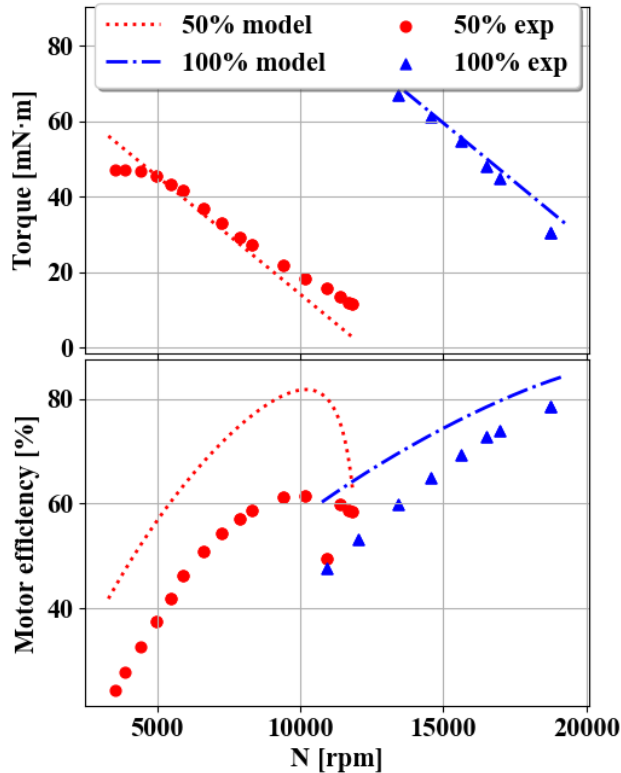


Figure 3.16: BLDC motor model v1 predictions ($V_{DC} = 10 \text{ V}$)

3.2.3 Accounting for harmonic losses

The theoretical models capture the experimental trends for torque and efficiency, but the accuracy of the models suffers from speed and throttle effects. The experimental torque values diverge from the predicted linear behavior at the extremes of the speed range while the efficiency model over-predicts motor efficiency over the entire speed range. The torque divergence at high speeds and the overall efficiency overprediction can be semi-empirically modeled with the current data. However, modeling the torque divergence from linear behavior at low speeds requires additional testing to determine if the torque taper is due to one or more of the following:

1. **Current limits:** the 360 W DC power supply and the power analyzer both have current limits of 20 A; therefore, motors were only loaded up to 20 A. The recent integration of 200 A current sensors and a 40 A power supply should remove this testing limit.

2. **Sub-optimal commutation:** the sensorless ESCs used in small electric UAS rely on back-EMF to sense the motor rotor's position and effectively commutate motor current. At low speeds, the motor generates insufficient back-EMF for optimum commutation and torque-production.
3. **Over-heating:** the magnetic field strength of permanent magnets drops significantly with heat [27]. Joule heating from high currents can create a positive feedback loop where heat reduces k_t and thereby torque and speed which forces the user to increase throttle to maintain a desired operating condition which further reduces k_t and requires more current until the motor is fried. Adding a motor cooling system to the dynamometer could mitigate this issue for short tests.

At high speeds, the inductance of the motor windings begin to considerably affect motor operation. Inductance is the tendency of a conductor to resist changes in current. Current must change polarity more rapidly with speed, so inductance grows with rotational speed and delays the flow of current in the motor that corresponds to an applied voltage. The delay due to inductance and a delay due to harmonic distortions from throttling contribute to an overall phase lag in the motor, (ϕ). The motor phase lag is calculated using the active power (P_{AC}) and apparent power (S) measured by the power analyzer (Eq. 3.13). Figure 3.17 plots motor phase lag versus speed for three throttle settings. The changing slope of motor phase lag versus speed is from inductance while the higher overall values of motor phase lag for lower throttle settings is from harmonic distortions. The inductance lag affects the torque-speed curve and will be used to empirically correct the torque model while the distortion lag affects efficiency and will be used to empirically correct the efficiency model.

$$\phi = \arccos\left(\frac{P_{AC}}{S}\right) \quad (3.13)$$

When the ESC applies a voltage across the windings during a commutation cycle at high speeds, the non-negligible inductance delays the flow of current which delays the formation of

a magnetic field by the windings which effectively reduces k_t . The lower k_t reduces the slope of the torque-speed curve and generates the divergence seen at high speed. Unfortunately, no small electric UAS component manufacturer provides data on motor inductance, so an empirical correction factor must be applied to account for its effects.

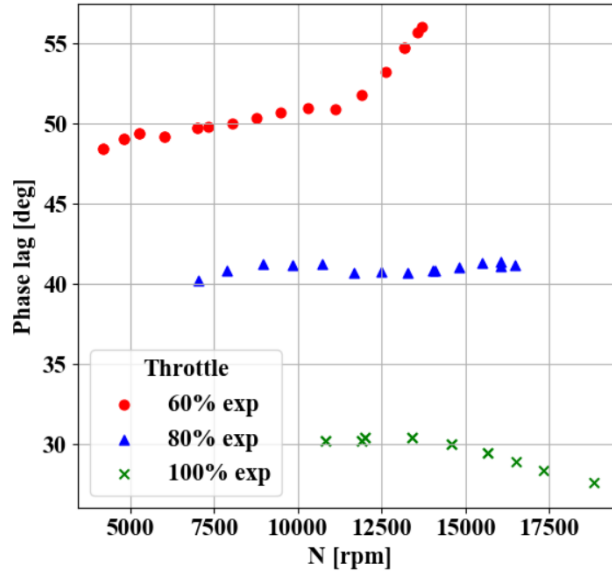
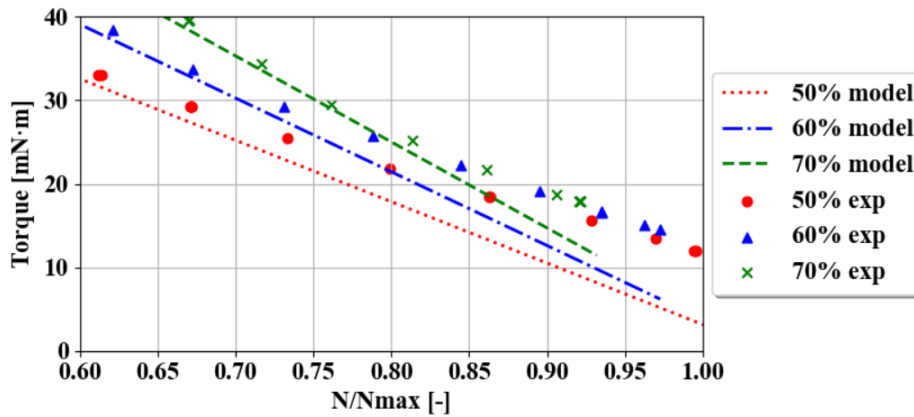


Figure 3.17: Motor phase lag versus shaft speed ($V_{DC} = 10$ V)

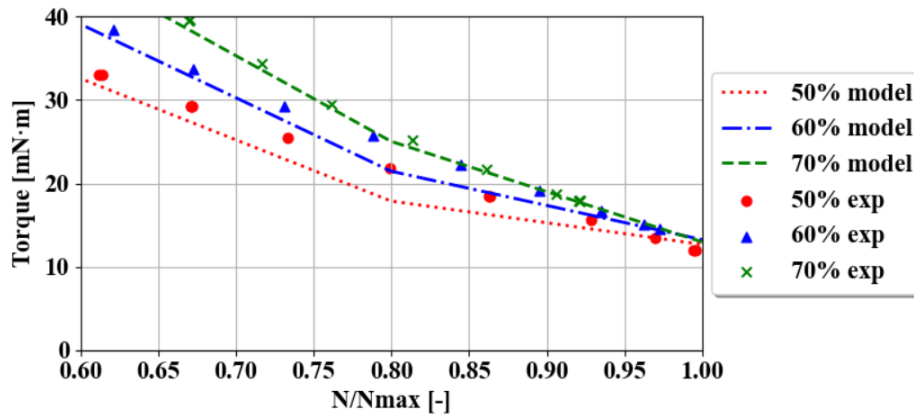
Experiments indicate that the high-speed divergence begins to occur at 75% of the maximum speed permissible by E , and this divergence more greatly affects low-throttle settings. In Eq. 3.14, a reduction factor c acts on k_t as a function of speed and duty ratio (throttle setting). Figure 3.18 compares the results of the empirical correction for 50–70% throttle settings. An exponential factor to d was chosen as to limit the impact to low throttle settings where d is not near unity. Note, the x-axis values for each plotted throttle setting have been normalized by the maximum speed permissible by back-EMF at that throttled voltage. Before the correction (top), the predicted torque for each throttle setting decreases at a constant rate and under-predicts torque at high speed. After the correction (bottom), the predicted torque decreases more slowly after 75% maximum speed and more closely follows the experimental divergence.

$$M_1 = \frac{V_{DC} d c k_t - (c k_t)^2 \omega}{R_m}$$

$$c = \begin{cases} 1 & \omega \leq 0.75 \omega_{max} \\ d^{1.5} & \omega > 0.75 \omega_{max} \end{cases} \quad (3.14)$$



(a) Theoretical torque-speed predictions (M_1)



(b) Semi-empirical torque-speed predictions (M_2)

Figure 3.18: BLDC motor model v3 torque predictions ($V_{DC} = 10 \text{ V}$)

Throttling voltage itself affects the electrical signals entering the motor regardless of speed. Fig. 3.19 displays oscilloscope readings of voltage (yellow) and current (cyan) across a motor phase. At 100% throttle (top), these waveforms generated by the ESC have relatively low noise,

but the waveforms carry significant noise from higher order harmonics at 50% throttle (bottom). The higher harmonics contribute to conduction and magnetization losses without generating any mechanical power. In order to correct for these harmonics losses, Equation 3.11 was modified to include a duty-ratio scaling function incorporated into the joule heating and iron loss terms. In the new efficiency model (Eq. 3.15), both terms are scaled inversely by duty ratio such that losses behave nominally at unity duty ratio (ideal throttling) while losses double as duty ratio approaches 50%. A 10% penalty was added to the mechanical output power term in the denominator to account for friction and magnetic hysteresis losses that are difficult to model per Ref. [27].

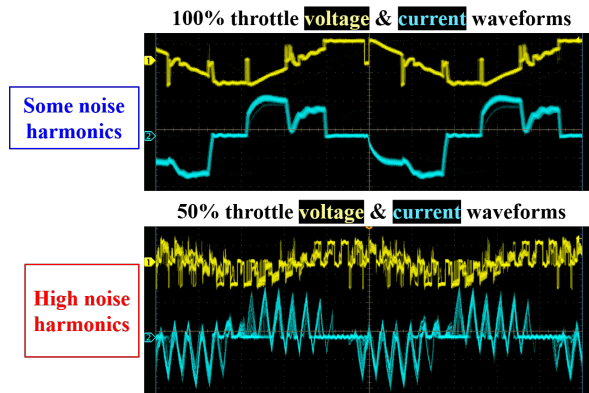
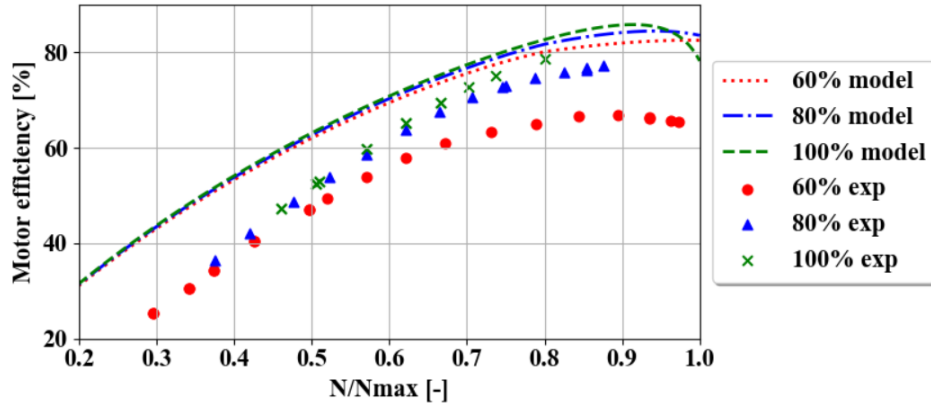


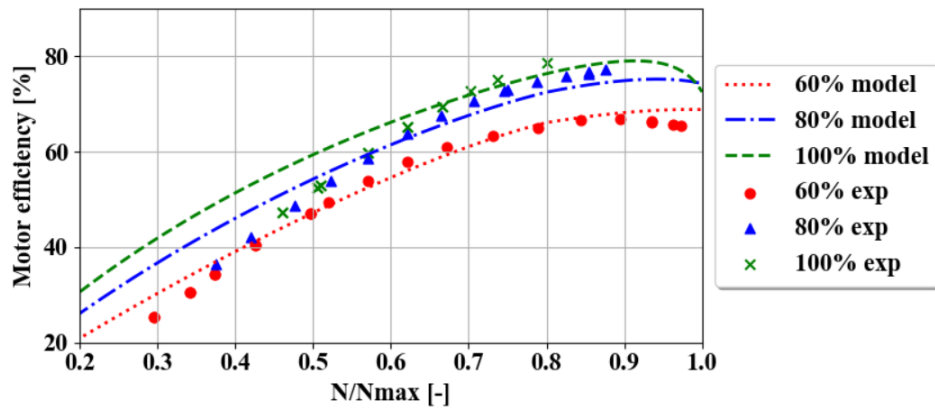
Figure 3.19: Motor plots, 100% throttle (top) and 50% throttle (bottom)

$$\eta_3 = \frac{M_1\omega}{1.1M_1\omega + (I^2R_m + k_t\omega I_0)/d} \quad (3.15)$$

Figure 3.20 shows the improvement in efficiency predictions between the theoretical model (top and Eq. 3.11) and the semi-empirical model (bottom and Eq. 3.15) for three throttle settings plotted over a normalized speed range. The overall efficiency curve for the new model suffers with lower throttle settings like experimental data.



(a) Theoretical efficiency predictions (η_2)



(b) Semi-empirical efficiency predictions (η_3)

Figure 3.20: BLDC motor model v3 efficiency predictions ($V_{DC} = 10$ V)

3.3 Sizing model

Compared to finding torque data, a more abstract and difficult barrier to this work was finding the right balance of empirical and physical methods to solve the inverse problem of motor sizing. Equation 3.5 provided a physical relationship between torque and size, but this expression relied on two other parameters that were only nominally independent. Moreover, electric machine literature provided no guidance for determining motor mass from volume. Reviews of motor design textbooks did yield insights that would inform the present work.

3.3.1 Initial attempts

Asked to design a motor for a given load, a motor designer will use eq. 3.5 and a few rules of thumb ($B \approx 1$ Tesla, $J \approx 10$ A/mm) to provide an initial best guess of the motor size [28]. The designer will then look to existing motors of similar size to ascertain more detailed information about the motor's geometry, such as the thickness of the stator teeth and the number of rotor magnets. The designer will use this data to develop a model of the motor in electromagnetic finite element analysis (FEA) software so that the designer can incrementally tweak the design to meet the desired output.

Initially in the sizing algorithm development process, the author sought to minimize empirical influences by replicating the traditional motor design process through purely analytical means. The author then explored electric machine literature for analytical models that could predict terms like B , J , and the number of poles for any given geometry. The search soon proved futile since motor designers themselves rely on empirical trends to develop initial estimates of these terms before switching to FEA tools. Moreover, these design parameters don't belong in a UAS design framework.

Instead, empirical methods can be used to extract details about the motor's external footprint from the stator size predicted in eq. 3.5. The additional information can then be used to accurately predict the motor's total mass. Consequently, a UAS conceptual design engineer may quickly evaluate various motor concepts as part of a larger UAS design sweep. If the conceptual engineer so chooses, he or she may relay the external specifications of the "ideal" motor predicted by the sizing algorithm to a motor designer for further development. Alternately, the vehicle engineer may pick the closest existing motor in a catalog.

3.3.2 Motor teardown

In an effort to understand how the different components of a motor change in size and mass as a function of the overall size and mass, three KDE motors of varying mass and aspect ratio ³

³Aspect ratio is defined as stator diameter versus length

were disassembled and studied. As pictured in Fig. 3.21, All of the motors consisted of a stator assembly, rotor assembly, and bearings. The stator assembly held the stator and its support and was easily separated into the two components. The rotor assembly held the permanent magnet ring, shaft, and support structure for the rotor and could not be easily separated into its constituent components.



Figure 3.21: BLDC motors of various size

Figure 3.22 plots each part's share of the total motor mass. From the 24 g motor to the 380 g motor, the relative stator mass increases by about 40% and the the relative rotor mass decreases by about 25% despite their closer aspect ratios (5.75 versus 9). This suggests that the mass algorithm should treat the motor as an assembly of changing parts rather than a lump mass. From the 24 g motor to the 98 g motor, aspect ratio decreases by more than half yet the relative mass of the active parts (rotor, stator) does not exhibit as drastic a change. Therefore, the mass algorithm should utilize aspect ratio as a guide to predicting the change in part masses.

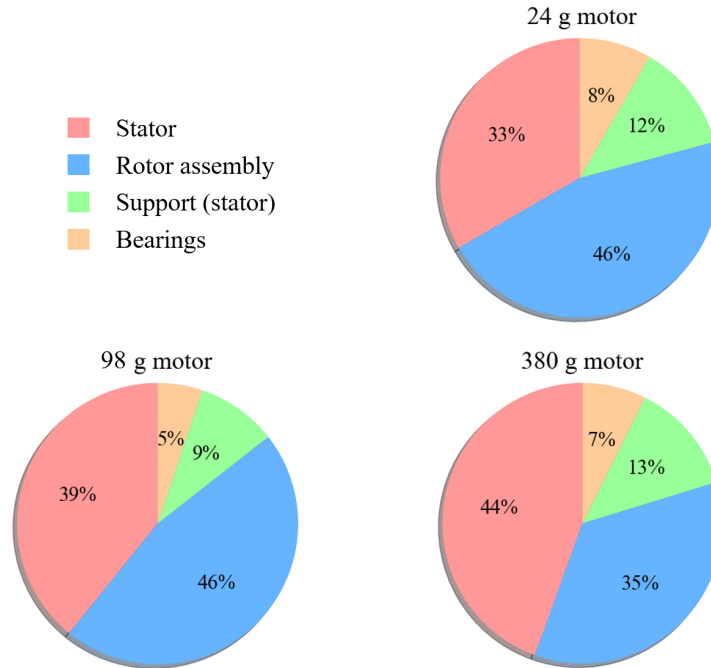


Figure 3.22: Motor mass breakdown

3.3.3 Prediction size and mass

Equation 3.5 provides a clear physical relationship between volume and torque, and the motor teardown revealed that the mass contributions of the active (windings, iron core, magnets, etc.) and passive (structural) components in the motor change with torque and aspect ratio. If the torque and mass is plotted with a color gradient that is a function of the stator's diameter/length aspect ratio (Fig. 3.23), then two linear data sets emerge: a series of low aspect-ratio motors up to about 700 g and 600 mN·m and a series of high aspect ratio motors between 400–1100 g and higher than 500 mN·m. This bifurcation agrees with the numerous tubular-shaped motors at the small–medium range of KDE's catalog and the flatter, pancake-shaped motors at the large range. The two linear regions are also apparent when torque is plotted against stator volume in Fig. 3.24.

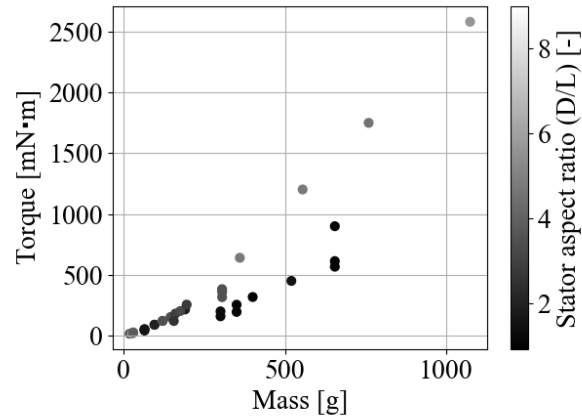


Figure 3.23: KDE catalog torque versus mass, aspect ratio

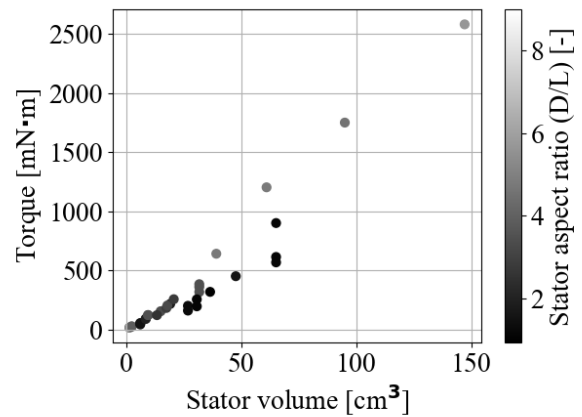


Figure 3.24: KDE catalog torque versus stator volume, aspect ratio

The constant slope of both linear regions in the torque versus stator volume plot suggests that shear stress is constant for each set. The higher shear stress for the wider aspect ratio motors may stem from increased magnetic flux densities and/or surface current densities for these geometries. However, the scope of the sizing study is limited to an aspect ratio of 4 since only four motors have higher aspect ratio geometries. Figure 3.25 plots these remaining motors, and its slope roughly

equates to $\sigma = 4.6$ kPa ignoring the point above 800 mN·m.

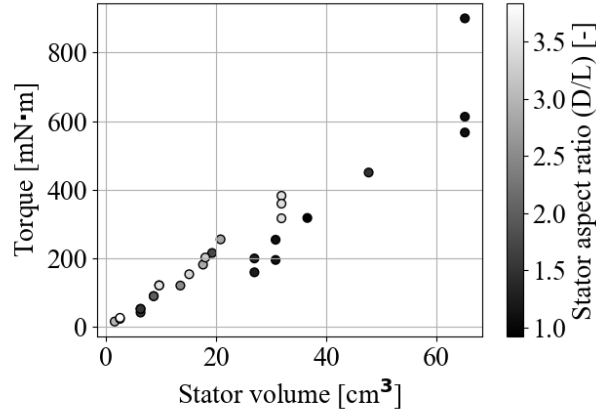


Figure 3.25: KDE catalog with aspect ratio limit of 4

The linear slope(s) of torque versus stator volume and torque versus total mass suggests that density may be defined and used to relate eq. 3.5 to mass. The strong effect of aspect ratio on the torque, size, and mass suggests using aspect ratio as the basis of an empirical study to develop details about the other components (rotor, support) not published in the catalog.

The motor teardown inspired us to take advantage of a motor's discrete components (stator, rotor, support) and develop a component model of cylinders that could build up the parts' mass contribution for any aspect ratio or torque as modeled in eq. 3.16. Figure 3.26 compares this component model to the actual components of the 380 g motor:

1. **Support:** The two support elements are as a solid cylinder with diameter D_o (the outer diameter of the motor) and density $\rho_{support}$. The length of a single support element is half the difference of the total motor length L_o and stator length L_s such that $L_{support} = \frac{1}{2}(L_o - L_s)$.
2. **Stator:** The stator is modeled as a solid cylinder with diameter D_s , length L_s , and density ρ_{stator} .

3. **Rotor:** The rotor is modeled as a hollow cylinder (tube) which sits concentrically outside the stator. The rotor is defined by inner diameter D_s , outer diameter D_o (the outer diameter of the motor), length L_s , and density ρ_{rotor}

$$m_{total} = 2m_{support} + m_{stator} + m_{rotor} \quad (3.16)$$

$$m_{total} = 2\rho_{support}U_{support} + \rho_{stator}U_{stator} + \rho_{rotor}U_{rotor}$$

$$U_{support} = \frac{\pi}{4}D_o^2 \frac{1}{2}(L_o - L_s)$$

$$U_{stator} = \frac{\pi}{4}D_s^2 L_s$$

$$U_{rotor} = \frac{\pi}{4}(D_o^2 - D_s^2)L_s$$

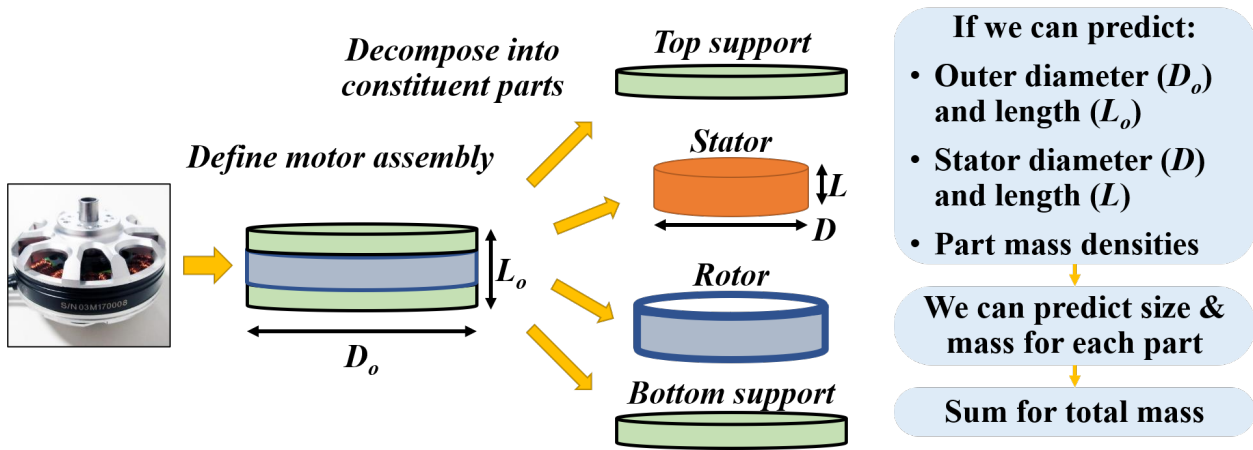


Figure 3.26: Overview of geometric mass model

Equation 3.5 can provide the stator volume given the required torque and the shear stress of KDE motors. Assuming aspect ratio is prescribed by the user or a higher-level design algorithm, the resulting stator volume and aspect ratio can provide stator diameter and length. At this point, logarithmic curve fits can be applied to relate the stator dimensions to the motor's outer dimensions

as a function of the motor's aspect ratio. Figure 3.27 plots the curve fit of stator and outer diameter, and Fig. 3.28 plots the curve fit of stator and outer length. Table 3.1 lists the corresponding component densities which were averaged between the three teardown motors.

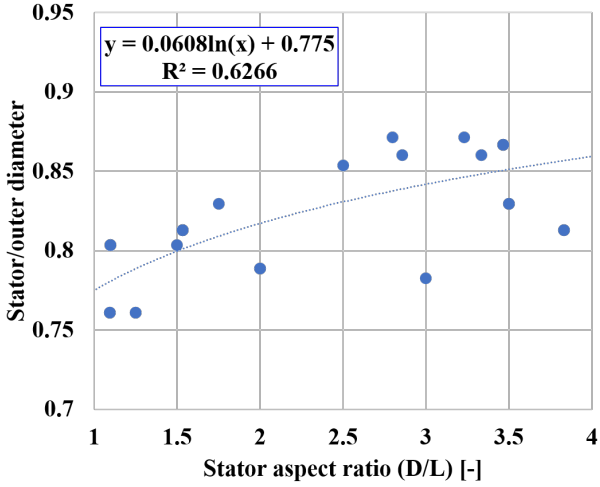


Figure 3.27: Diameter ratio versus aspect ratio

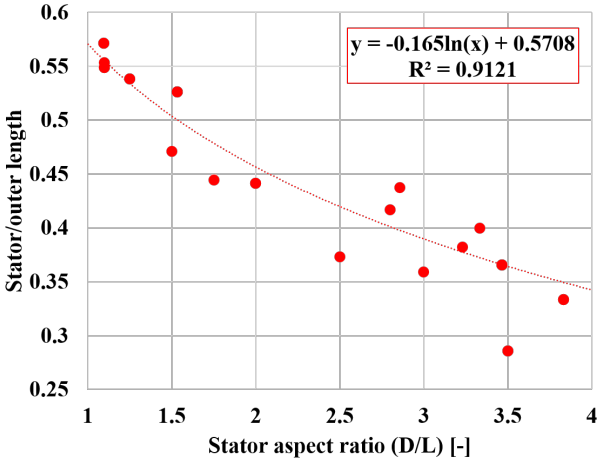


Figure 3.28: Length ratio versus aspect ratio

Table 3.1: Component densities averaged across 3 motor sizes

Component	Averaged density [g/mm ³]
Support	0.85
Stator	4.80
Rotor assembly	9.10

Figure 3.29 illustrates how the theoretical torque-volume expression in eq. 3.5, the theoretical component model, and the empirical geometric studies combine to form a semi-empirical sizing algorithm to predict mass from torque. The subsequent figures incrementally apply layers of the algorithm, beginning with the final volume-to-mass prediction, against KDE's catalog to examine error and uncertainty propagation.

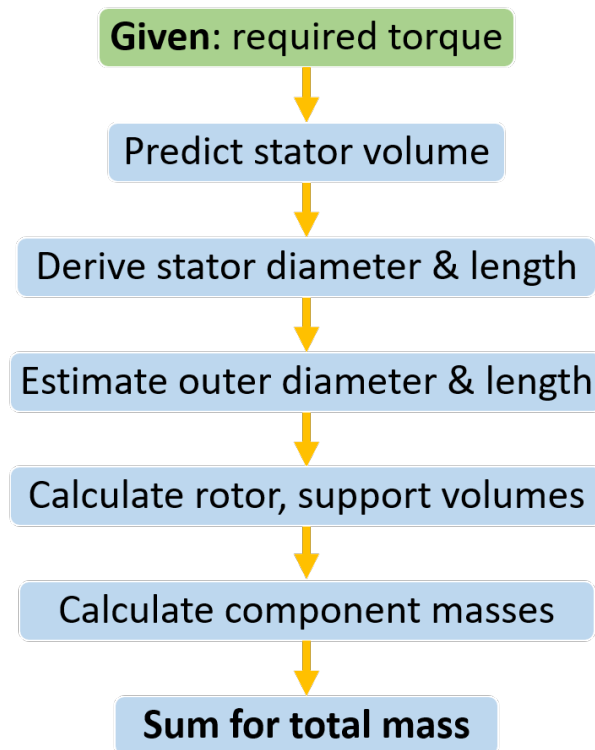


Figure 3.29: Mass-prediction algorithm flow chart

Figure 3.30 plots the algorithm's predictions when given the stator diameter, stator length, outer diameter, and outer length. This figure shows the accuracy of predicting motor mass using idealized component volumes and empirically-derived densities. The predictions trend very well, especially at small scale.

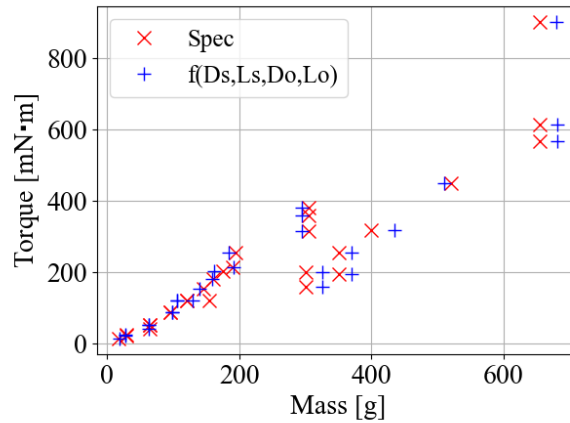


Figure 3.30: Mass prediction given stator and outer dimensions

Figure 3.31 plots the algorithm's predictions given the stator diameter and stator length. This figure also factors the accuracy of the empirical studies, which predict the outer geometry of the motor. The data still trends well especially around 300 g.

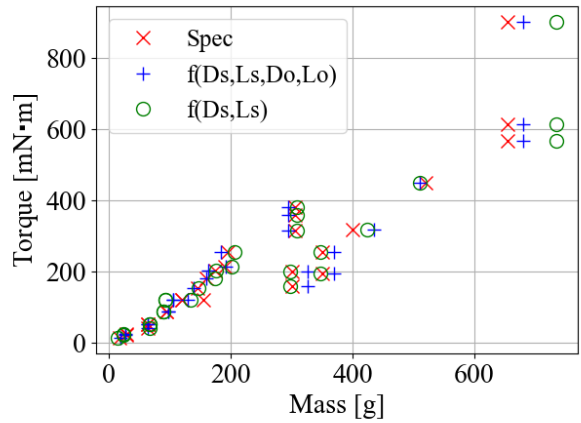


Figure 3.31: Mass prediction given stator dimensions

Figure 3.32 plots the algorithm’s predictions given torque and aspect ratio. This figure shows the full accuracy of the semi-empirical algorithm. The data trends well for small motors, but the error accumulation above 600 g/600 mN·m is about twice the actual value. This large mass/high torque outlying prediction reflects the fact that the shear stress and empirical studies were sized with more numerous low-aspect ratio data.

This figure shows the full accuracy of the semi-empirical algorithm. The data trends well for small motors, but the error accumulation above 600 g/600 mN·m is about twice the actual value. This large mass/high torque outlying prediction reflects the fact that the shear stress and empirical studies were sized with more numerous low-aspect ratio data.

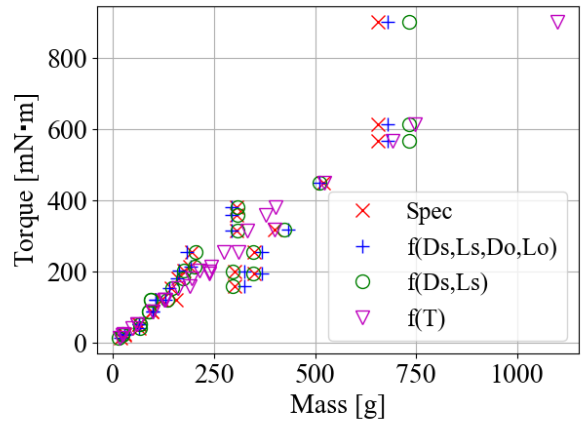


Figure 3.32: Mass prediction given torque and aspect ratio

The mass of 10 motors from a different manufacturer (*Scorpion Power Systems*) were predicted using the KDE-tuned mass algorithm. Again, this catalog did not provide any torque data, so the motors' rated torque was estimated using Scorpion's max current ratings. Figure 3.33 plots the algorithm's mass predictions. Although the sizing algorithm was not expected to perform well given a set of data with wholly different (unknown) thermal cutoffs, the sizing algorithm still trended very well.

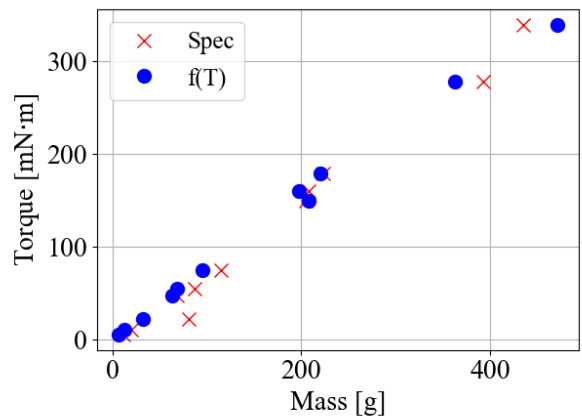


Figure 3.33: Mass prediction of independent catalog

3.3.4 Predicting electrical constants

Equivalent circuits can model the natural steady state torque versus speed performance of a BLDC motor at various voltage and throttle settings using the torque constant⁴ k_t and resistance R . A function of k_t and R called k_m can also be used as a figure of merit to compare motors of the same size. This *motor constant* is defined in eq. 3.17 and quantifies how well a motor's active components (windings, core, magnets, etc.) convert current into useful torque rather than wasteful heat. Therefore, it is advantageous to be able to predict these constants for any motor so that an equivalent circuit model can validate the performance of the conceptual motor.

$$k_m = \frac{M}{\sqrt{I^2 R}} = \frac{k_t I}{I \sqrt{R}} = \frac{k_t}{\sqrt{R}} \quad (3.17)$$

Note that k_m is not a dimensionless ratio that can be used to compare motors of differing size. Rather, k_m is a measure of how well a motor's inner design converts current to torque at any given point. For example, two motors of the same size may have winding wires of different gauge (wire diameter). The motor with a wider gauge will have lower resistance R (and thereby bear more current), but each stator tooth will have less wires around it because each wire takes up more space. These teeth will not generate as much electromagnetic forces per unit charge, so the torque constant k_t will decrease. Ultimately, the decrease in R and decrease in k_t will cancel to a net zero change in k_m , but the thinner gauge motor may be more suitable for a current-limited setting.

The constant nature of k_m for changes in wiring stems from magnetic relations which are beyond the scope of this paper⁵. For motor application purposes, it suffices to note that a motor's k_m will not change for different winding configurations *iff* the bare copper volume inside the motor does not change. On the other hand, re-configuring the copper wiring does enable the motor to operate more effectively for different electrical settings, such as the aforementioned thin-gauge motor suited for low-current.

⁴Recall that the speed constant k_v is the inverse of the torque constant, so calculating one constant will fix the other.

⁵See Hanselman sec. 4.10 [29]

Rather than attempt to predict all of the constants independently, a motor's external connections, such as the input voltage, and the configuration-independent k_m , can be leveraged to prescribe the optimal electrical configuration for a given size. The input to this function would be the desired speed, applied voltage, and the geometry predicted earlier in the sizing algorithm. The output of this function would be the optimal electrical constants. These constants would then be fed into a performance model to evaluate the motor's performance with respect to motor requirements and supply data to other framework models, such as motor current data for the battery model.

Recall that k_t and k_v are inverses of each other. The rate at which a motor converts current to torque is equal to the rate at which the motor develops speed from voltage. If the motor is operating near max speed (and thereby, peak efficiency), and some initial voltage is prescribed, then the optimal speed constant can be fixed to yield efficient performance at that voltage. Equation 3.18 shows this calculation as well as the conversion to the optimal torque constant. If a k_m figure is known, the desirable R of the motor can be solved for by re-arranging eq. 3.17 and plugging in the known k_m and optimal k_t . The challenge thus becomes predicting a realistic figure of merit for a motor of a given size.

$$k_v = N_{desired}/V_{system}[\text{rpm/V}] \quad (3.18)$$

$$k_t = \frac{60}{2\pi k_v}[\text{N}\cdot\text{m/A}]$$

Hanselman [29] derives an expression for k_m as a function of the motor's magnetic flux density B , stator diameter D_s , bare copper volume U_{Cu} , and copper's electrical resistivity ζ (eq.3.19). Assuming the magnetic flux density and electrical resistivity are constant at nominal conditions, this expression may be reduced to a function of D_s and U_{Cu} . Assuming volume of bare copper in a motor is a fraction of the stator volume U_{stator} , k_m can be approximated as a power function of the two variables predicted by the mass algorithm as expressed in eq. 3.20.

$$k_m = \frac{1}{2}BD_s\sqrt{\frac{U_{Cu}}{\zeta}} \quad (3.19)$$

$$k_m \propto D_s\sqrt{U_{Cu}} \propto D_s^{a_1}U_{stator}^{a_2} \quad (3.20)$$

Regression of a quarter of the KDE catalog against this power expression yields exponent values close to Hanselman's theory: $a_1 = 0.88$ (1.00 in theory) and $a_2 = 0.54$ (0.50 in theory). Figure 3.34 plots k_m predictions made for the entire KDE catalog. The inputs to the k_m model were the stator diameter and stator volume predicted by the mass sizing algorithm, and the outputs are co-plotted against the actual KDE values. The data trends well despite errors in the mass algorithm upstream. Figure 3.35 uses these k_m predictions and the catalog-provided k_t to predict the motor's resistance R . Again, the predicted values closely match the catalog specs despite upstream errors in the k_m and geometry predictions.

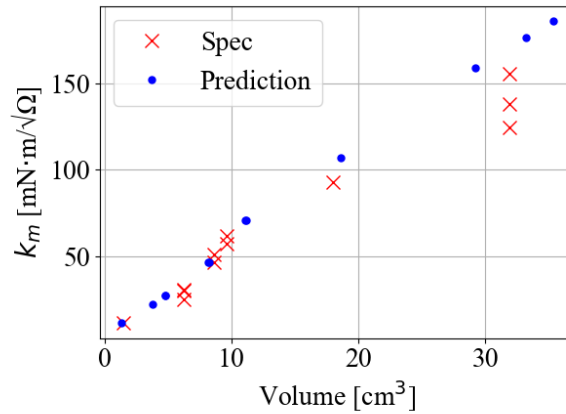


Figure 3.34: k_m predictions

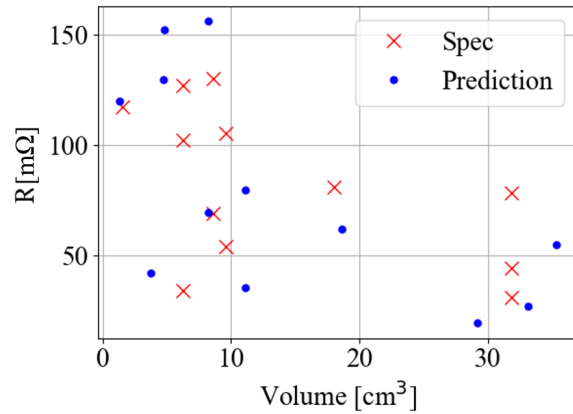


Figure 3.35: R predictions

As another test, the figure of merit and resistance of 10 motors were predicted from a second manufacturer's catalog (Scorpion Power Systems). Figures 3.36 and 3.37 plot the k_m and R predictions respectively for the second manufacturer. Because the the sizing algorithm's mass and geometry predictions had performed so well upstream, these downstream electrical constant predictions also trended very well.

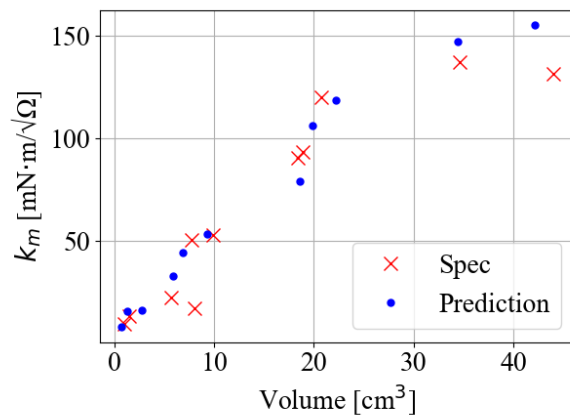


Figure 3.36: k_m prediction for independent catalog

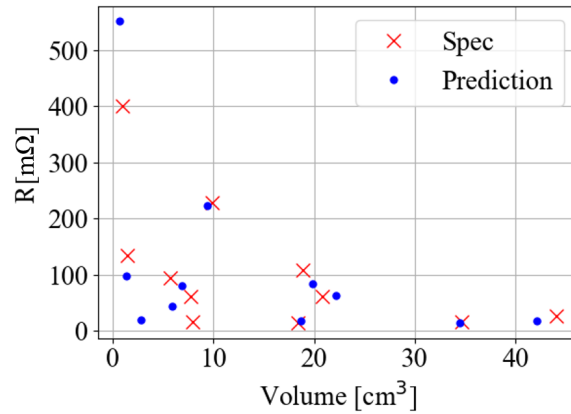


Figure 3.37: R prediction for independent catalog

3.4 Case study: High-speed versus high-torque motor

The different relations of motor size and performance can be seen when comparing a high-speed motor to a high-torque motor. Table 3.2 lists the specifications of two such motors both rated for about 7 kW (9.4 hp) of power. The high-speed motor has almost half the mass of the high-torque motor (655 versus 1075 g), so the high-speed motor has almost double the specific power (11 versus 6.7 kW/kg). However, the high-torque motor can deliver almost triple the maximum torque of the high-speed motor, so the high-torque motor has a higher specific torque (6.9 versus 12 N·m/kg). Each is better suited for different applications.

Table 3.2: Comparison of high-speed and high-torque motors⁶

Motor type	High-speed	High-torque
Mass [g]	655	1075
Stator aspect ratio (D/L)	1.1	5.7
Rated power [kW]	7.2	7.4
Max torque [N·m]	4.5	12.9
k_t [mN·m/A]	32.4	90.9
R [m Ω]	18	23
k_m [$\frac{\text{N}\cdot\text{m}}{\sqrt{\Omega}}$]	0.241	0.600

In applications where maximum power is important, such as land-based racing where the maximum *vehicle* speed is a function of motor power, then the high-speed motor should be used to minimize motor mass for a required power output. Moreover, combining the high-speed motor with a single-stage transmission to reduce the load torque on the motor will also reduce copper losses for a required power output and enable the motor to operate more efficiently. This is partly why most electric cars still have a single-stage transmission. A motor is more responsive and efficient than an internal combustion engine, but:

1. a motor still has some losses which waste battery power
2. a battery stores an order of magnitude less usable energy per unit mass than gasoline (0.72 versus 9.2 MJ/kg for a lithium-ion battery versus gasoline)

On the other hand, in applications where a transmission is undesirable for its added weight or mechanical complexity, then the high-torque motor is more advantageous. For the same amount of current, the high-torque motor delivers almost triple the torque of the high-speed motor as denoted

⁶KDE models 700XF-295-G3 (high-speed) and 10218XF-105 (high-torque)

by their differences in k_t (90.9 versus 32.4 mN·/A). Moreover, the high-torque motor develops this torque with less losses since its k_m is more than double the k_m of the high-speed motor (0.241 versus 0.600 units). The larger figure of merit even stands when normalized by mass (k_m/mass): the high-torque motor has a “specific k_m ” of about 0.55 units versus the high-speed motor’s specific k_m of about 0.38 units. The high-torque motor enjoys these advantages in part due to its wider aspect ratio. The magnetic interactions between the stator and rotor travel through a longer moment arm for “free” and thereby increase the torque output for the same current input.

Note that the high-torque motor will suffer from a higher moment of inertia thanks to its wider aspect ratio [30]. This means that the high-torque motor will respond more sluggishly to transient commands. Moreover, the high-torque motor cannot even achieve the same shaft speeds as the high-speed motor because of its “torque-y” design. The higher k_t value that generates a larger torque per unit current also generates a higher back-EMF per shaft revolution. Therefore, the high-torque motor will encounter its electrical speed limit (when back-EMF equals the input voltage) at a lower shaft speed for the same input voltage. These and other tradeoffs which are beyond the scope of this work are why motor selection is such a critical part of electric vehicle design and why the models developed in this thesis can help identify and engineer solutions for these issues.

3.5 Summary

The presented work only examines performance and efficiency of sensorless BLDC motors for small UAS. However, the following principles can be applied to BLDC motors of any size:

1. ***Limit torque is a function of current and limit speed is a function of voltage:*** For a motor with fixed specifications (such as k_t), the maximum achievable speed is limited by the input voltage and the maximum achievable torque is limited by the input current.

Without an applied load, the motor’s maximum rotational speed will be limited by back-EMF, and the only way to overcome this limit is to ensure that the input voltage is greater than the back-EMF voltage. With a load, the maximum speed will probably be limited by the torque necessary to spin the load at a given speed. In that case, the maximum attainable

speed becomes a maximum producible torque problem which is limited by input current even if the input voltage is greater than the back-EMF generated at the desired speed.

2. **Motor drive systems achieve high efficiency close to the no-load speed:** Unlike combustion powertrains, electric powertrains can deliver high torque at low speeds without a transmission. In fact, a motor with perfect commutation will produce maximum torque at zero speed. However, low speed operating states—relative to the maximum no-load speed—are the most inefficient state because of the nature of joule heating losses.

Joule heating losses, which dominate at low speed, grow by current squared, and since current is linearly proportional to torque, joule heating losses grow by torque squared. Iron losses, which dominate at high speeds, grow by speed. Assuming the motor trades torque for speed linearly, less power will be lost at high speed.

3. **Motor size is driven by torque, not power:** For a standard “can” motor, the output torque is linearly proportional to length and quadratically proportional to diameter. Since a motor’s speed limit is a function of supplied voltage, a small (low-torque) motor operated at high voltage can deliver just as much power as a large (high-torque) motor operated at low voltage. eVTOL engineers seeking a direct drive solution should first examine a motor’s rated torque—not the rated power—as manufacturers will often advertise the power achieved through high-speed/low-torque operation.

4. **Motor torque is limited by the environment:** A motor generates torque with current, and current *rapidly* generates heat through I^2R losses. This heat can melt insulation between wires and cause a short, or it can heat the motor’s magnets beyond their Curie point at which the magnets will demagnetize. Therefore, eVTOL engineers should always monitor a motor’s thermal state and compare data against the manufacturer’s stated boundaries. Aerospace engineers should take note that electrical time constants are on the order of micro- and milliseconds, so a motor can “instantly” fail just as it can “instantly” deliver torque. Therefore, any high torque operation beyond a few minutes requires active liquid cooling.

5. **Motor efficiency increases with diameter:** Motor torque is linearly proportional to current and quadratically proportional to diameter. The heat generated by I^2R losses of current is the primary source of power loss in a motor. At the same current and at the same speed, a larger diameter motor will generate more torque and thereby more power. This is why small hobby BLDCs realistically achieve efficiencies up to 80% while larger eVTOL motors achieve efficiencies greater than 90%. Therefore, eVTOL engineers should strive to select wider diameter motors when permissible.

6. **Motors can be wound to meet electrical constraints:** A motor's footprint is largely set by the output torque requirement, but the inner design of the wires and iron core can be tweaked to account for the available input voltage and current as long as the bare copper volume (figure of merit) inside the motor does not change. For example, safety regulations may limit an eVTOL vehicle to a system voltage of 300 V, but a suitable motor for the vehicle is rated to operate at 600 V. The motor manufacturer can re-wind the motor to operate efficiently at 300 V, albeit with a higher current.

4. ELECTRONIC SPEED CONTROLLER

4.1 Primer

Motor drives, or “Electronic Speed Controllers” (ESCs) in hobby parlance, are part power converter, part controller. The ESCs consist of six metal-oxide-semiconductor field-effect transistor (MOSFET) switches that selectively complete a connection between two windings and the DC source to generate current in the motor. ESCs can vary the voltage by pulse-width modulation (PWM) of the DC source voltage [31].

The ESC must energize the windings at the right time to maintain optimal orientation between the stator and rotor magnetic fields. Industrial BLDC drivers and “sensored” hobby ESCs use hall sensors on the motor shaft to track the revolving rotor, but “sensorless” ESCs use back-EMF to track the rotor. Sensorless drive simplifies motor construction and weight at the cost of more complex driver electronics and degraded performance at low speeds where motors generate insufficient back-EMF for optimum control [32].

The motor-ESC interplay is generalized in Fig. 4.1. Each sub-figure consists of a DC source on the left, six switches in the middle, and three windings on the right (Fig. 4.1.a). In Fig. 4.1.b, switches 1 and 5 are closed which completes a circuit between the battery terminals and windings A and B. The resulting current creates a “north” stator field which the “east” rotor field pursues. The ESC observes the changing back-EMF on winding C as the fields interact to extract rotor position. The ESC pulses switch 1 on/off at duty ratio, d , to vary the voltage across windings AB as $+dV_{DC}$ where d is also the non-dimensional form of the user’s throttle setting. When the rotor field nears the stator field of this commutation cycle, the ESC opens both switches and closes switches 2 (PWM) and 4 (full) to generate the next cycle (Fig. 4.1.c) when the process is repeated. Intermediate steps have been omitted and field orientations simplified for clarity.

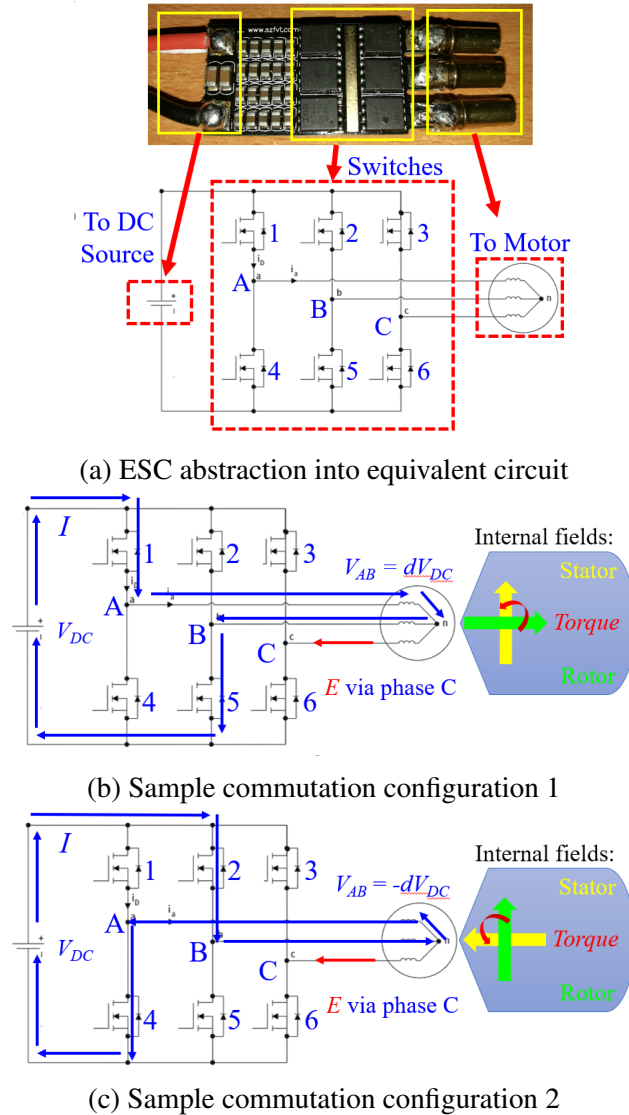


Figure 4.1: Simplified ESC commutation example (author figure)

Instantaneously, only a single phase of current enters the motor despite the presence of three windings, so the brushless motor performs like a brushed “DC motor”. The ESC is externally changing (commutating) the DC current’s polarity to lead the rotor field. Macroscopically, the waveforms travelling across the motor wires look like three AC waveforms, so accurately capturing the electric power entering a BLDC motor requires a three-phase power analyzer. Note that the usable electric power entering the motor (“active power”, P_{AC}) is not the simple product of the root-mean-square voltage and current in these three AC lines (“apparent power”, $S \propto V_{RMS}I_{RMS}$).

The active power is the sum of the *instantaneous* product of voltage and current across the three phases ($P_{AC}(t) = v(t)i(t)$), which is what the power analyzer is designed to measure.

The same motor and driver hardware can work under true three-phase principles if the ESC drives three currents into the motor. This type of motor drive system is generally known in the electric machine community by the “synchronous motor” (sync) designation and delivers smoother torque compared to BLDC systems. Miniature sync drive systems were not developed for the hobby RC market due to high development costs for the synchronous motor control algorithms. However, larger and higher performing electric aircraft, such UAS weighing 200 lb. (90 kg) or more will benefit from synchronous drive systems’ more rigorous technical literature and finer controls [33, 34].

4.2 Performance models

At any time, a single phase of current travels to the motor via two of six ESC switches. One switch is always on (closed) and acts like a conductor while another switch is pulsed on/off at a duty ratio to throttle voltage. Both switches have some non-ideal resistance. Therefore, the six-switch ESC equivalent circuit of Fig. 4.1 can be abstracted into a single throttling switch and 2 resistors. The equivalent circuit in Fig. 4.2 shows such an abstracted ESC connecting a voltage source on the left (V_{DC}) with a current source (I) on the right. The voltage source represents the DC power source while the current source represents the current load drawn by the motor (and predicted by Eq. 3.12). The resistors (R_{sw}) represent the resistance of the two switches. When the PWM switch is on at some duty ratio d , the voltage at the load is scaled down by d which is essentially the operation of a voltage step-down converter (aka, Buck converter) [35].

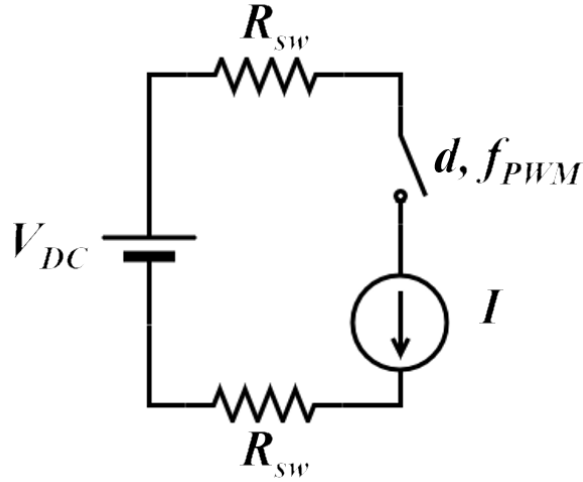


Figure 4.2: Reduced-order equivalent circuit

Buck converters are well documented in power electronics literature [36]. Equation 4.1, an expression for ESC efficiency, can be derived from the circuit shown in Figure 22 4.2. $P_{in,m}$ is the AC power predicted by the motor model, P_{cond} (Eq. 4.2) is power lost to conduction across the switch resistances, P_{sw} (Eq. 4.3) is extra power lost to the PWM switch during its transition period (T_{trans}) between ON and OFF states, and P_{Qi} is the quiescent power of the ESC. No ESC manufacturer any specifications of the ESC switches, so order of magnitude estimates were used for R_{sw} , T_{trans} , and P_{Qi} from Ref. [36]. The PWM switching frequency (f_{PWM}) is a user setting on the KDE ESC used in this study (8–32 kHz) and was set to 18 kHz. Note that a distortion correction factor of $1/d$ has been applied to the conduction losses just as in the motor model.

$$\eta_3 = \frac{P_{in,m}}{P_{in,m} + P_{cond} + P_{sw} + P_{qi}}, P_{qi} = 5 \text{ W} \quad (4.1)$$

$$P_{cond} = (2R_{sw}I^2)/d \quad (4.2)$$

$$P_{sw} = V_{DC}If_{PWM}T_{trans} \quad (4.3)$$

The values predicted by Eq. 4.1 are compared to experimental values in 4.3 along the normalized speed axis for different throttle settings. The model captures the overall increase in efficiency from higher throttle settings and a peak in efficiency around 85 percent maximum speed. However, none of the coefficients of any loss term in the ESC efficiency model are manufacturer provided specifications, so only the prediction trends may be trusted. In addition to changing PWM frequency, software options in the ESC can modify features like commutation timing, so more tests of different ESCs operating at different software settings is needed to confidently model the ESC [37].

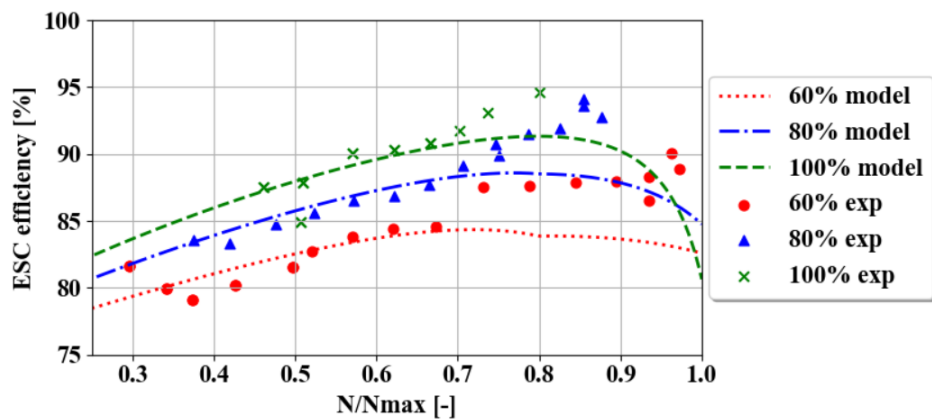


Figure 4.3: ESC efficiency predictions ($V_{DC} = 10 \text{ V}$)

4.3 Hover stand validation

The combined motor torque, motor efficiency, and ESC efficiency models were integrally tested in a practical loading condition using a commercial 3-bladed, 4.5 inch (11.5 cm) diameter small electric UAS rotor. The rotor is recommended to be paired with 2S (8 V) – 3S (12 V) systems, so an average 10 V operating voltage was selected for the hover stand tests. The system was commanded 50–100 percent throttle in 5 percent increments, and the same suite of sensors used in the dynamometer setup recorded the same parameters listed in Fig. 2.2. The recorded steady-state speeds at which the motor drive system spun the rotor load were then used as inputs for

the combined motor+ESC model to predict the system's performance at the recorded states. The results of the motor torque, driver current, and total efficiency are plotted versus speed in Fig. 4.4. Data for 95 and 100 percent throttle has been omitted due to resonance at their corresponding speeds.

All three prediction curves correlate well with experiment. The largest difference between experimental and predicted values is in the current drawn by the ESC at low speeds wherein predicted current is consistently higher than the experimental current. The ESC is the least-understood component of the powertrain model because of the ESC's "blackbox" software algorithms. Future characterization of the ESC under different software settings should improve current predictions. Conversely, the largest deviation between the predicted and experimental for total efficiency is only five percent at low speeds which suggests the presented semi-empirical framework is viable. In fact, the average value of 60 percent total efficiency—far below the popular assumption of 90 percent efficiency for electric powertrains—befits extensive use of the developed models to quickly explore whether a more efficient selection of components and operating conditions will not potentially waste half the battery's energy.

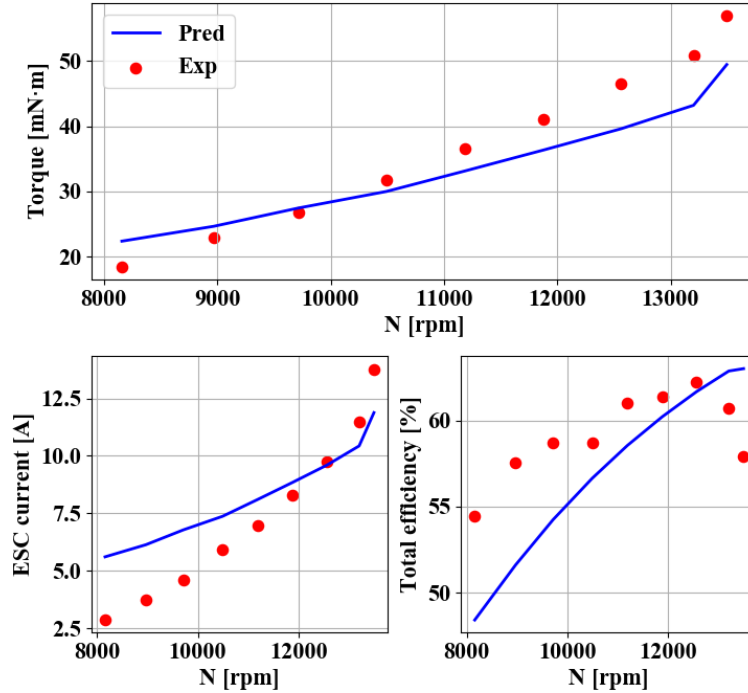


Figure 4.4: Hover stand predictions ($V_{DC} = 10$ V, 50–90 percent throttle)

4.4 Summary

The scope of this work is limited to six-step commutation motor inverters/controllers. However, the physics based approach which yielded the present models enables us to apply the following principles to a motor inverter/controller of any size or architecture:

1. **Throttling reduces driver and motor efficiency:** In every commutation cycle, a driver must expend energy to activate a certain path for motor current. To throttle voltage within that cycle, the driver must expend extra energy to repeatedly clip excess voltage, and this clipping distorts the voltage and current waveforms with high frequency noise. Real power is generated when voltage and current align. If the waveforms do not align due to noise, then some power is lost.

This principle is also true for true 3-phase sinusoidal, field-oriented control (FOC) motor controllers used to drive larger and more powerful permanent magnet synchronous motors

(PMSM) in full-scale electric VTOL vehicles. In these settings, operating at partial throttle (modulation index < 1) will also generate harmonic noise in the motor.

2. ***Solely increasing available power by increasing operating voltage can decrease overall efficiency:*** Conventional wisdom advises increasing voltage to decrease current and I^2R losses, but the first principle (torque as function of current) discussed earlier suggests the drawn current will not change for a given load torque. Moreover, the third discussed trend (throttling decreases voltage) suggests that limiting extra voltage wastes energy across the driver and motor. Therefore, increasing voltage will increase total losses.

This misconception doubly impacts small electric UAS during powertrain sizing. For example, a quadcopter design requires 100 W of power from the power source for 10 min. of hover with a motor drive system operating rated for the design load point at a rated DC voltage of 8 V. This equates to 16 Watt-hours (Wh) of energy or 2 Ampere-hours (Ah) of capacity. An application engineer may be tempted to choose a 16 V, 1 Ah battery to reduce current across the system, but principle 3 (throttle reduces efficiency) suggests energy will be needlessly wasted as the motor driver throttles at 50 percent (8 V to motor) to operate at the design load. Instead, the engineer should select a 12 V, 1.33 Ah battery that provides the same energy with lower losses as well as a margin for excess voltage and current for high performance maneuvers. The models presented here could immediately validate this and other hypothesis without the need for additional testing.

5. BATTERY

5.1 Primer

Batteries are the most common power source for small electric UAS. Connecting a load to the battery terminals completes a path between two partitions, or electrodes, of differing chemical composition in the battery cell. A relative difference in electric potential (voltage) between these two electrodes drives the flow of positive ions across a separator between the partitions and negative electrons across the load that gradually equalizes the cell's potential difference. The load draws power from the moving electrons and can accelerate the time to equilibrium. The reaction rate also decreases as ions are depleted on one side which translates into a voltage that decreases with a cell's discharged capacity. Figure 5.1 shows a simplified battery cell that relies on lithium ions. Note that the capacity, or electric charge stored by the chemical reactants, increases with the mass of reactants in the cell, but the voltage is defined by the selection of chemical reactants themselves and will not change with mass [38].

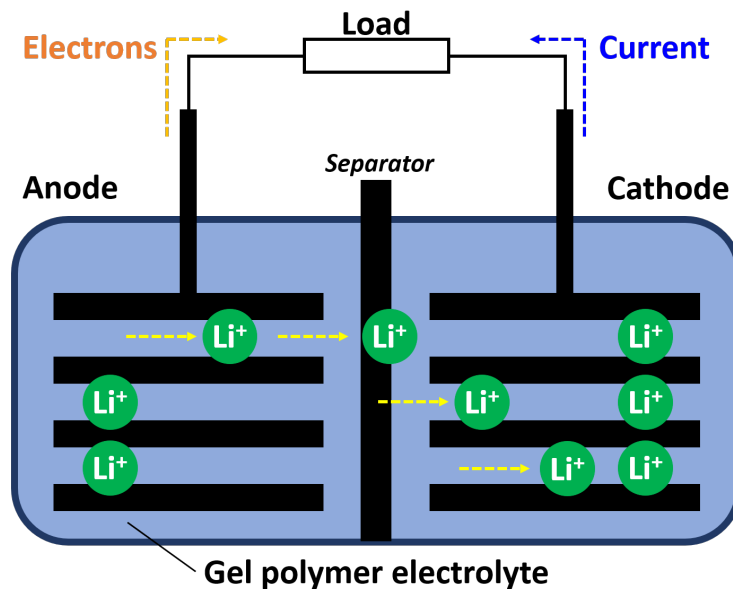


Figure 5.1: Lithium-ion battery diagram (author figure)

Different reactants have different reaction rates and electric potentials, so each chemistry will have a unique curve for the variation in chemical voltage versus discharged capacity ($Q_{discharged}$, Eq. 5.1) [39]. These curves are typically normalized in the x-axis by the cell's rated capacity (Q_{rated}) to generate voltage versus non-dimensional “depth of discharge” (DOD , Eq. 5.2) or “state of charge” (SOC , Eq. 5.3) plots. DOD is a measure of a cell's relative discharged capacity, and SOC is the complementary measure of a cell's relative remaining capacity.

$$Q_{discharged}(t) = Q_{discharged_{t=0}} + \int_0^t i(\tau) d\tau \quad (5.1)$$

$$DOD(t) = Q_{discharged}(t)/Q_{rated} \quad (5.2)$$

$$SOC(t) = 1 - Q_{discharged}(t)/Q_{rated} \quad (5.3)$$

These capacity-agnostic plots enable intuitive comparisons of different chemistries, as shown in Fig. 5.2 for three common chemistries. The near-triple area-under-the-curve (energy) of lithium's curve versus nickel-metal hydride's curve underscores lithium's domination of the battery market. Other chemistries still offer some benefits not visible in this graphic, such as lead-acid chemistry's higher peak discharge limit which is critical to starting engines [40].

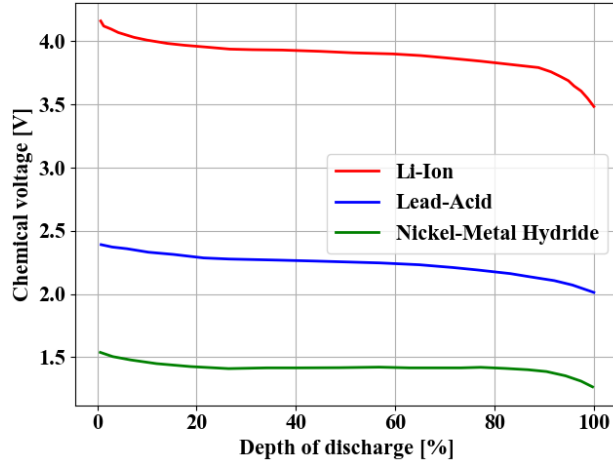


Figure 5.2: State of charge (SOC) plots of common battery chemistries

A battery pack consists of cells wired in series to increase pack voltage (V) or in parallel to increase capacity (Q): a pack of 2 cells in series or parallel is called a 2S or 2P battery respectively. The capacity rating is from the nominal current output of the pack in 1 hour: a Li-ion pack that delivers 500 mA from full-charge voltage to a cutoff voltage for 1 hour has 500 mAh of rated capacity. The maximum voltage of a Li-ion cell is chemically limited at 4.2 V, but the lower voltage limit depends on a user's battery lifetime requirements. Lower cutoff voltage will degrade performance, and a cutoff voltage of 3.3 V is widely used in the RC community. A pack's maximum current rate is noted by the "C-rating" ($C = I_{max}/Q_{rated}$) which is listed without dimensions even though it has units [1/time]. A sample 20C rating for the 500 mAh pack yields a maximum current of 10 A over 3 min (1/20 hr), but almost all chemistries' performance suffers above 2C.

The dynamic output/constant mass behavior of batteries means electric aircraft do not get lighter with time like combustion-powered aircraft. Therefore, accurately modeling a small electric UAS' mission performance requires a powertrain model that captures the battery's dynamic output as a function of time and the applied load.

5.2 Performance model

Unlike a combustion engine which delivers the same specific power at full and at near-empty fuel, a battery will deliver more specific power at full charge than at near-empty charge. Thus, the battery model must capture the component's time-varying performance. An equivalent circuit model by Abu-Sharkh and Doerffel [41] capitalizes on each chemistry's unique chemical voltage versus depth of discharge (*DOD*) curve to dynamically predict terminal voltage as a function of drawn current. The full circuit is shown in Fig. 5.3.

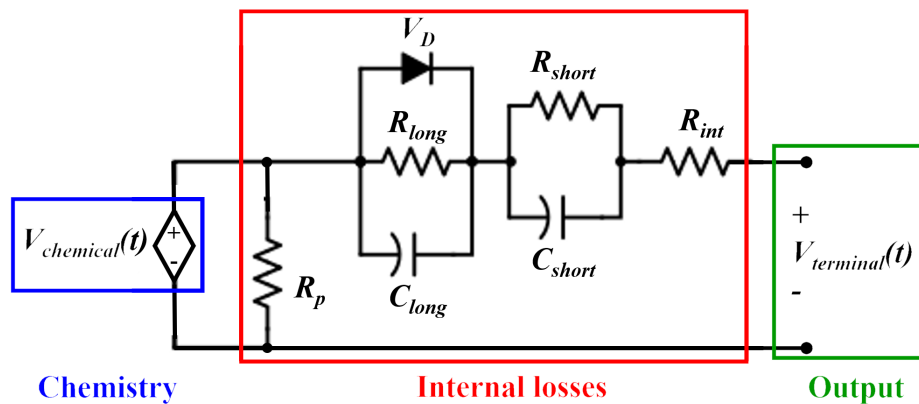


Figure 5.3: Abu-Sharkh and Doerffel battery equivalent circuit

This circuit separates the chemically-driven voltage source inside a battery, the battery's internal loss sources, and the output voltage seen at the battery terminals. The dynamic DC source on the left ($V_{chemical}$) generates voltage as a function of time or voltage as a function of *DOD* if the drawn current is always known. Since voltage versus *DOD* is fixed for each chemistry (see Fig. 5.2), this element provides the underlying voltage curve for any size (capacity) battery of a given chemistry.

A mixture of resistors, diodes, and capacitors in the middle of the circuit model impedances that reduce the chemical voltage into the output voltage seen at the terminals. Resistance R_p models a cell's tendency to self-discharge. Resistance-capacitance pairs "long" and "short" model

AC transients that activate when the battery is discontinuously discharged. Diode V_D models hysteresis between charge and discharge curves. Resistance R_{int} models the internal resistance of the battery that increasingly hampers voltage output at high discharge rates (see Fig. 2.4).

The inherent use of small electric UAS powertrains permits significant simplification of this circuit. Li-ion cells used for almost all small electric UAS applications self-discharge over weeks, so R_p can be eliminated. The voltage change across RC networks is proportional to time derivative of current, but the near-instant changes in throttle yield relatively small voltage drops across the RC networks, especially compared to the much larger voltage drop across R_{int} . Therefore, both transient sub-circuits can be eliminated ¹. Diode V_D , which Ref. [43] indicates is 68 mV throughout discharge, can be merged with $V_{chemical}$. Thus, the 8-element circuit in Fig. 5.3 reduces to the 2-element circuit in Fig. 5.4.

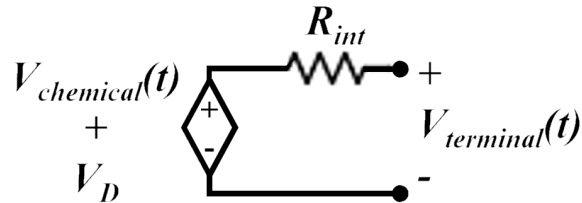


Figure 5.4: Reduced-order battery equivalent circuit

Applying Kirchhoff's Voltage Law to this circuit yields Eq. 5.4, a prediction of battery terminal voltage at any moment in time. The expression for $V_{chemical}$ 5.5 is an empirical fit provided by Ref. [43] for a Lithium chemistry's chemical voltage versus state of charge (or DOD) curve. If $i(t)$, the instantaneous current drawn by the load, and R_{int} are known, then Eq. 5.4 can be solved to obtain output voltage versus time for a constant or dynamic current discharge. Figure 5.5 graphs terminal voltage per cell versus DOD predicted by this model at 2C and 4C constant discharge for a 2S, 610 mAh battery alongside the respective experimental curves. Predicted values were ± 5 percent

¹These sub-circuits *are* important for life cycle analysis [42]

of measured values throughout discharge.

$$V_{terminal}(t) = V_{chemical}(t) + V_D - i(t)R_{int} \quad (5.4)$$

$$V_{chemical}(t) = k + b_1 e^{ax} + b_2 x - b_3 x^2 + b_4 x^3$$

$$x = SOC(t), k = 3.685, a = -35$$

$$b_1 = -1.031, b_2 = 0.2156$$

$$b_3 = -0.1178, b_4 = 0.3201$$
(5.5)

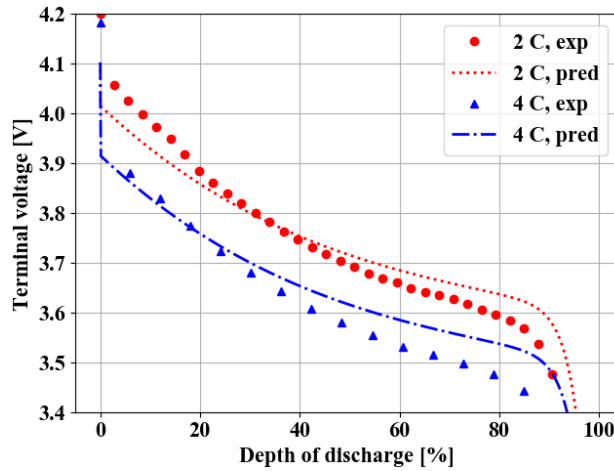


Figure 5.5: Battery model predictions (2S, 610 mAh)

5.3 Benchtop internal resistance measurement

Some battery manufacturers provide internal resistance, but a single benchtop experiment can also extract R_{int} and $V_{chemical}(t) + V_D$ for any battery. Note from Fig. 5.4 that voltage is lost across R_{int} only when current flows. Otherwise (when current is zero), $V_{terminal}(t) = V_{chemical}(t)$. If a cell's terminal voltage is continuously measured while square wave pulses of current are drawn from the cell, then R_{int} and $V_{chemical}(t) + V_D$ can be extracted from the plot of $V_{terminal}(t)$.

Figure 5.6 plots terminal voltage (top) and drawn current (bottom) for a pulsed discharge test of a 1300 mAh RC Li-ion battery with an unknown R_{int} . The current is a square wave with an amplitude of 1.3 A (1C of the battery), period of 1 min, and a duty ratio of 75 percent. That means current is drawn in 1 minute cycles of 1.3 A for 45 seconds and 0 A for 15 seconds. Overall, the terminal voltage generally trends down, but the terminal voltage momentarily increases during the off-portion of the discharge cycle when current is zero. These terminal voltage "hills" are a glimpse into the internal battery dynamics.

Figure 5.7 is a closer look at two such hills. When current stops flowing, no voltage is lost across R_{int} and the terminal voltage begins to climb towards $V_{chemical}(t)$. Connecting the peak voltages of these hills in terminal voltage will yield a time history of $V_{chemical}(t) + V_D$ that can be modified into an *SOC* or *DOD* curve using Eq. 5.3 and Eq. 5.2 respectively. Dividing the sharp slope of the hills by the amplitude of current yields a time history for R_{int} that stays constant down to approximately 20% *DOD* at which point the battery should not be discharged any further. References [43] and [41] discuss the estimation of the other elements of the full battery model (Fig. 5.3) using the same pulsed test procedure. Such deeper characterization may be needed for the analysis of electric powertrains of vehicles with operating dynamics that significantly activate the elements ignored for small electric UAS powertrain analysis.

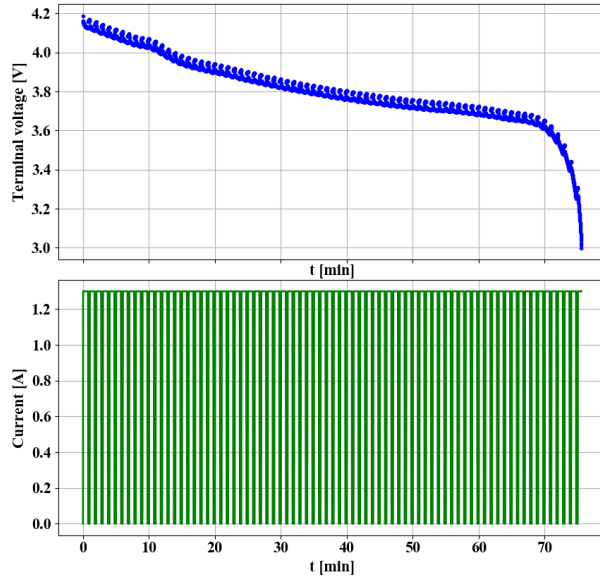


Figure 5.6: Pulse-discharge terminal voltage (top) and drawn current (bottom)

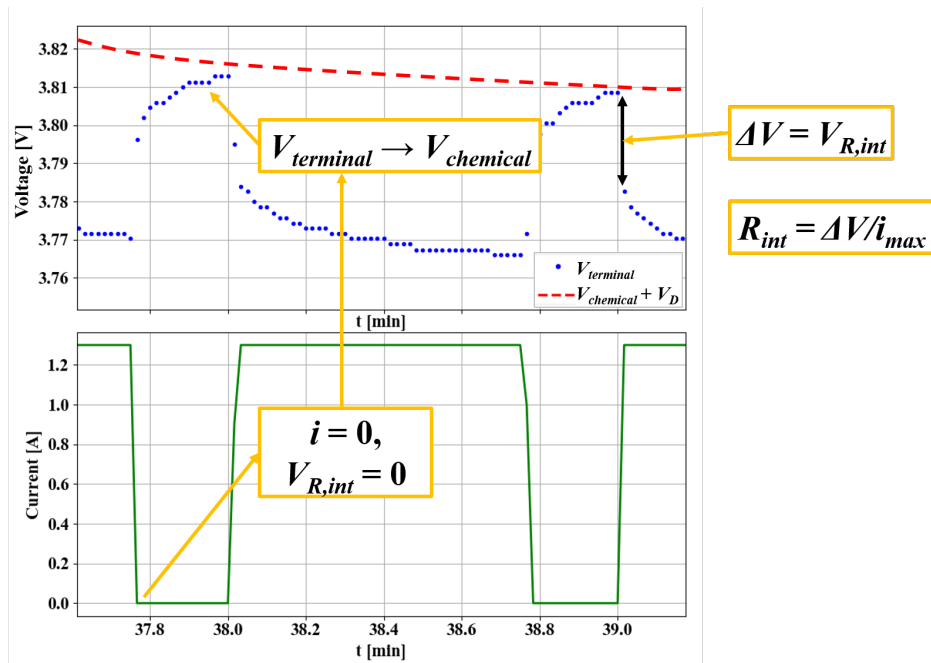


Figure 5.7: Zoomed pulse-discharge plot

5.4 Summary

The battery is perhaps the single most stringent limiting factor for electric flight at any scale. A battery does not contain as much energy per unit mass as combustion fuels, nor does the battery get lighter with time—both of which hinder applications for the mass-sensitive world of flight. Moreover, a battery's energy density will *decrease* with higher discharge rates as the higher current generates more internal losses. This is a double-penalty for electric *vertical* flight wherein power is required to constantly overcome drag *and* lift (in a fixed-wing, the wing overcomes lift "for free"). Therefore, the battery's output voltage and temperature must be carefully monitored across the *entire* duration of an EVTOL vehicle mission to ensure satisfactory—let alone, optimal—performance. The model presented here enables this necessary analysis.

6. CONCLUSION

6.1 Summary

In this work, performance and sizing models are developed to aid conceptual design and optimization of the electric powertrain for small unmanned aerial systems based on an outrunner brushless DC motor ¹ architecture. The performance models can predict the steady-state behavior of the motor, motor controller (electronic speed controller, or ESC), and the battery using high-level component specifications provided by RC hobby part manufacturers. The sizing model can predict the optimal motor size, mass, and electrical constants for desired steady-state torque and shaft speed.

6.1.1 Performance model summary

The performance models can predict the output torque and shaft speed of a powertrain configuration and the efficiency of each powertrain component at any load point using only two or three high-level specifications. The performance predictions were validated against experimental data collected from a custom dynamometer, 3-phase power analyzer, and a battery analyzer.

1. The motor performance model can predict output torque within 10% of experimental values and motor efficiency within 5% of experimental values in the nominal shaft speed range ²
2. The ESC performance model can predict the ESC efficiency within 10% of experimental values in the nominal shaft speed range
3. The battery performance model can predict the battery's voltage versus time (state of charge) for a time-varying load within 5% of experimental values

The accuracy of the models depends on the accuracy of the manufacturer's component specs (such as the "true" battery capacity), but the models can provide accurate physics-based feedback of

¹More rigorously known as a radial-flux, outer-rotor, permanent-magnet synchronous motor

²When the motor shaft speed generates sufficient back-EMF for the ESC to properly sense and control the motor

how changing each component parameter affects overall the powertrain performance. If certain parameters are re-configured, the models can also be applied towards modeling of land- and sea-based electric vehicles with similar-sized brushless DC powertrains.

The following general principles for powertrains based on brushless DC motors were deduced from experimental trends, model behavior, and operating physical principles:

1. **Max torque is a function of current and max speed is a function of voltage.** Torque is nominally proportional to current, so running a motor on a current-limited power source (such as a benchtop power supply) will limit the maximum achievable torque regardless of the available voltage. Similarly, output speed is nominally proportional to the applied voltage, so running a motor on a voltage-limited power source (such as a battery at low voltage) will limit the max motor speed regardless of throttle setting.
2. **Motor drive systems achieve high efficiency close to the maximum no-load speed** since I^2R losses, which tend to dominate other losses, trend to zero as the growing speed generates higher back-EMF in the windings that then limits input current.
3. **Throttling reduces driver and motor efficiency** by introducing higher-order harmonic noise into the voltage and current waveforms which do not contribute to real output power.
4. **Solely increasing available power by increasing operating voltage can decrease overall efficiency** if the motor controller has to throttle down the operating voltage to achieve a desired "low" speed.

6.1.2 Sizing model summary

In addition, the work derived an outrunner brushless DC motor sizing algorithm consisting of theoretical models tuned by empirical studies. Given the operating torque and speed and a prescribed aspect ratio, the algorithm can predict the mass, figure of merit k_m , speed constant (aka, voltage constant) k_v ³, and resistance R .

³The torque constant k_t is related to the speed constant by $k_t = \frac{30}{\pi k_v}$

1. For a given torque, the sizing model can predict motor mass within 5% for sub-1 kW BLDC motors popular in small UAS
2. Using these mass calculations, the sizing model can also predict motor figure of merit (k_m) within 10%
3. For a given shaft speed and voltage, the sizing model can tune the motor's speed and torque constants (k_v and k_t) and derive an order of magnitude estimate for the motor's resistance

The algorithm was validated against a technically rigorous catalog of more than 30 motors, and the following principles were deduced that can be applied to size brushless DC motors:

1. **Motor size is driven by torque, not power.** Power is equal to torque times speed. Torque is proportional to motor volume, but speed is nominally limited by voltage—a non-mechanical parameter. Therefore, a small, high-speed motor can deliver as much—if not more—power as a large, high-torque motor.
2. **Motor torque is strongly limited by available cooling.** High torque operation requires high current, and the resulting heat is quadratically proportional to the current. Therefore, a high-torque motor will need powerful cooling mechanisms to ensure safe and continuous operation.
3. **Motor efficiency increases with diameter.** The magnetic forces that generate torque act at the lateral surface area between a motor's stator and rotor. Increasing the diameter increases the moment arm of these interactions and thereby "freely" increases the resulting torque without adverse effects.
4. **Motors can be re-wound to meet electrical constraints.** The torque (mechanical) requirements of a motor drive its outer size, so naturally the electrical requirements of a motor will drive its inner design, such as the number of wire turns per stator winding and the number and shape of the rotor magnets. To an extent, this variability enables a motor designer to freely adjust the inner design for high-voltage/low-current, medium-voltage/medium-current, or

low-voltage/high-current environments without any changes in the output torque and efficiency versus speed.

6.2 Contributions to literature

This work attempts to address a knowledge gap in the aerospace community of how electric machines perform at different conditions using physics-based models and component specifications—not empirical test data. The semi-empirical performance models of the motor, motor controller, and battery enable a vehicle designer to analyze a powertrain’s performance across the vehicle’s entire mission profile with a more accurate estimate of how the components will respond at non-ideal conditions. This stands in contrast to existing works which rely on static assumptions about motor efficiency or can only predict performance at pre-tested data points.

The motor sizing algorithm addresses an even larger knowledge gap by solving the inverse problem of finding the optimal motor for a desired operating condition. This semi-empirical set of models provides a vehicle designer a more nuanced answer compared to existing design tools that rely on purely statistical trends. Namely, while statistical fits can reasonably predict a motor’s mass for a given torque, they cannot go beyond and predict this hypothetical motor’s electrical constants since these parameters require a physical connection between the desired torque, the predicted size, and the available electrical supply. The presented sizing algorithm can bridge this gap.

6.3 Future work

This work has provided a strong conceptual *and* hands-on understanding of electric machines and electric powertrains for aerospace applications. Nevertheless, the author would like to address gaps in this work and expand the scope of the work by addressing the following issues through doctoral studies.

6.3.1 Re-vamped hoverstand testing

Modifying the hoverstand to accept a larger and more powerful variety of motors will enable the author to validate the motor and ESC performance models across a wider range of operating conditions and components. Upgrading the hoverstand to measure motor and ESC temperature

will provide data to inform, expand, and validate the motor sizing algorithm as well as to develop a sizing algorithm for the ESC. Running sustained hoverstand tests using **battery power** will also yield data to validate the battery performance model and to develop battery sizing models.

6.3.2 Other architectures

Heavier, sensed brushless DC motors used in terrestrial RC cars and boats can run at slower speeds and higher torques than the lighter, sensorless BLDCs used in aerial RC vehicles. Testing the models against these motors would enable the application of the presented models for land and sea-based systems as well. The author is particularly interested in how the sizing algorithm will change for *inrunner* (inner-rotor) sensed motors. This work could inform development of performance and sizing models of distinctly different architectures such as induction or reluctance motors, or even axial-flux motors.

6.3.3 ESC and battery sizing models

Compared to BLDC motors, a much narrower variety of ESC and batteries exist for small UAS. ESCs vary only in their current ratings, and batteries vary only in their voltage and capacity ratings. However, the author is interested in developing physics-based sizing models for these components, if only to guide similar work for alternate architectures, such as motor controller sizing for induction or reluctance motors.

6.3.4 Thermal modeling

Compared to combustion powertrains, electric powertrains suffer from a temperature sensitivity that is common to all of the components of an electric powertrain. Practically speaking, a motor that exceeds its temperature limits is far likelier to suffer immediate critical failure compared to an engine that experiences a similar ratio of over-temperature versus nominal temperature status. Therefore, practical and widespread adoption of these models by industry depends on developing thermal management models to accurately account for each component's thermal state.

6.3.5 Modeling at larger scales (> 1 kW)

Many generations of small UAS have already saturated a wide range of industries, so many users will opine that their potentially sub-optimal vehicle delivers "good enough" performance. However, larger fixed-wing and rotary-wing electric aircraft are only just coming off the drawing boards, and these first-gen systems will transition to market at a much slower rate. Therefore, expanding the scope of this work to larger size and power scales will greatly enhance the conceptual design and optimization of these full-scale vehicles and enable the the best design to reach market faster.

REFERENCES

- [1] M. D. Moore and B. Fredericks, “Misconceptions of electric propulsion aircraft and their emergent aviation markets,” 2014.
- [2] D. Coleman, M. Benedict, V. Hrishikeshavan, and I. Chopra, “Design, development and flight-testing of a robotic hummingbird,” in *71st annual forum of the American Helicopter Society*, American Helicopter Soc. Virginia Beach, VA, 2015.
- [3] C. C. Runco, B. Himmelberg, and M. Benedict, “Experimental studies on a mesoscale cycloidal rotor in hover,” *Journal of Aircraft*, vol. 56, no. 2, pp. 597–606, 2019.
- [4] H. Denton, M. Benedict, H. Kang, and V. Hrishikeshavan, “Development of a gun-launched rotary-wing micro air vehicle,” in *Vertical Flight Society 75nd Annual Forum and Technology Display*, 2019.
- [5] Federal Aviation Administration, “Faa drone registry tops one million,” 2018.
- [6] UAS Task Force Airspace Integration Integrated Product Team, “Department of defense unmanned aircraft system airspace integration plan,” tech. rep., Department of Defense, 2011.
- [7] J. Winslow, M. Benedict, V. Hrishikeshavan, and I. Chopra, “Design, development, and flight testing of a high endurance micro quadrotor helicopter,” *International Journal of Micro Air Vehicles*, vol. 8, no. 3, pp. 155–169, 2016.
- [8] S. Bhattacharya, V. Nagaraju, L. Fiondella, E. Spero, and A. Ghoshal, “Rotorcraft tradespace exploration incorporating reliability engineering,”
- [9] C. Justin, A. Ramamurthy, N. Beals, E. Spero, and D. Mavris, “On-demand small uas architecture selection and rapid manufacturing using a model-based systems engineering approach,”
- [10] W. Johnson, “Ndac-nasa design and analysis of rotorcraft,” 2015.

- [11] T. Du, A. Schulz, B. Zhu, B. Bickel, and W. Matusik, “Computational multicopter design,” *ACM Trans. Graph.*, vol. 35, pp. 227:1–227:10, Nov. 2016.
- [12] A. Cheng, Z. Fisher, R. Gautier, K. Cooksey, N. Beals, and D. Mavris, “A model-based approach to the automated design of micro-autonomous multirotor vehicle systems,” in *American Helicopter Society 72nd Annual Forum and Technology Display*, 2016.
- [13] B. Govindarajan, A. Sridharan, and I. Chopra, “A scalability study of the multirotor biplane tailsitter using conceptual sizing,” in *American Helicopter Society 74th Annual Forum and Technology Display*, 2018.
- [14] A. Sridharan, B. Govindarajan, and I. Chopra, “A scalability study of the multirotor biplane tailsitter using conceptual sizing,” *Journal of the American Helicopter Society*, vol. 65, no. 1, pp. 1–18, 2020.
- [15] W. Johnson, C. Silva, and E. Solis, “Concept vehicles for vtol air taxi operations,” 2018.
- [16] W. Johnson, “Ndarc-nasa design and analysis of rotorcraft validation and demonstration,” 2010.
- [17] R. A. McDonald, “Electric propulsion modeling for conceptual aircraft design,” in *52nd Aerospace Sciences Meeting*, American Institute of Aeronautics and Astronautics, jan 2014.
- [18] E. S. Hamdi, *Design of small electrical machines*. John Wiley & Sons, Inc., 1994.
- [19] S. Huang, J. Luo, F. Leonardi, and T. A. Lipo, “A comparison of power density for axial flux machines based on general purpose sizing equations,” *IEEE Transactions on energy conversion*, vol. 14, no. 2, pp. 185–192, 1999.
- [20] J. Mevey, “Sensorless field oriented control of brushless permanent magnet synchronous motors,” Master’s thesis, Kansas State University, Manhattan, NY, 2009.
- [21] A. Hughes and W. Drury, *Electric motors and drives: fundamentals, types and applications*. Newnes, 2013.
- [22] W. Soong, “Sizing of electrical machines.” Power Engineering Briefing Note 9, 9 1993.

- [23] S. Dunkl, *Control aspects of single and three phase PM drives in fractional power applications*. PhD thesis, Ph. D. dissertation, Electric Drives and Machines Institute, Graz University . . . , 2016.
- [24] J. R. Hendershot and T. J. E. Miller, *Design of brushless permanent-magnet machines*. Motor Design Books, 2010.
- [25] F. Saemi, M. Benedict, and N. Beals, “Semi-empirical modeling of group 1 uas electric powertrains,” in *Vertical Flight Society 75nd Annual Forum and Technology Display*, 2019.
- [26] T. A. Burress, S. L. Campbell, C. Coomer, C. W. Ayers, A. A. Wereszczak, J. P. Cunningham, L. D. Marlino, L. E. Seiber, and H.-T. Lin, “Evaluation of the 2010 toyota prius hybrid synergy drive system,” tech. rep., Oak Ridge National Lab.(ORNL), Oak Ridge, TN (United States), 2011.
- [27] H. A. Toliyat and G. B. Kliman, *Handbook of electric motors*. CRC press, 2018.
- [28] H. Toliyat. Email correspondence, March 2020.
- [29] D. C. Hanselman, *Brushless permanent magnet motor design*. The Writers’ Collective, 2003.
- [30] T. A. Lipo, *Introduction to AC machine design*. John Wiley & Sons, 2017.
- [31] D. G. Holmes and T. A. Lipo, *Pulse width modulation for power converters: principles and practice*, vol. 18. John Wiley & Sons, 2003.
- [32] T.-H. Kim and M. Ehsani, “Sensorless control of the bldc motors from near-zero to high speeds,” *IEEE transactions on power electronics*, vol. 19, no. 6, pp. 1635–1645, 2004.
- [33] S. W. Colton, *Design and prototyping methods for brushless motors and motor control*. PhD thesis, Massachusetts Institute of Technology, 2010.
- [34] D. W. Novotny and T. A. Lipo, *Vector control and dynamics of AC drives*, vol. 41. Oxford university press, 1996.

- [35] A. M. Hava, R. J. Kerkman, and T. A. Lipo, "A high-performance generalized discontinuous pwm algorithm," *IEEE Transactions on Industry applications*, vol. 34, no. 5, pp. 1059–1071, 1998.
- [36] "Power loss calculation with common source inductance consideration for synchronous buck converters," tech. rep., Texas Instrument, Dallas, 2011.
- [37] P. Damodharan and K. Vasudevan, "Sensorless brushless dc motor drive based on the zero-crossing detection of back electromotive force (emf) from the line voltage difference," *IEEE Transactions on Energy Conversion*, vol. 25, no. 3, pp. 661–668, 2010.
- [38] Y. Gao, M. Ehsani, and J. M. Miller, "Hybrid electric vehicle: Overview and state of the art," in *Proceedings of the IEEE International Symposium on Industrial Electronics, 2005. ISIE 2005.*, vol. 1, pp. 307–316, IEEE, 2005.
- [39] L. Gao, S. Liu, and R. A. Dougal, "Dynamic lithium-ion battery model for system simulation," *IEEE transactions on components and packaging technologies*, vol. 25, no. 3, pp. 495–505, 2002.
- [40] M. Ehsani, Y. Gao, and J. M. Miller, "Hybrid electric vehicles: Architecture and motor drives," *Proceedings of the IEEE*, vol. 95, no. 4, pp. 719–728, 2007.
- [41] S. Abu-Sharkh and D. Doerffel, "Rapid test and non-linear model characterisation of solid-state lithium-ion batteries," *Journal of Power Sources*, vol. 130, pp. 266–274, may 2004.
- [42] B. Saha, K. Goebel, S. Poll, and J. Christophersen, "Prognostics methods for battery health monitoring using a bayesian framework," *IEEE Transactions on instrumentation and measurement*, vol. 58, no. 2, pp. 291–296, 2008.
- [43] M. Chen and G. Rincon-Mora, "Accurate electrical battery model capable of predicting run-time and i–v performance," *IEEE Transactions on Energy Conversion*, vol. 21, pp. 504–511, jun 2006.